

Discussion Paper | Discussion Paper | Discussion Paper | Discussion Paper

10, 24499–24561, 2010

## T. Fan and O. B. Toon

## T. Fan and O. B. Toon

Received: 30 September 2010 – Accepted: 7 October 2010 – Published: 20 October 2010

Correspondence to: T. Fan (tianyi.fan@colorado.edu)

Published by Copernicus Publications on behalf of the European Geosciences Union.

Title Page

## Abstract

## Introduction

## Conclusions

## References

## Tables

## Figures



▶



[Back](#)

Close

Full Screen / Esc

[Printer-friendly Version](#)

## Interactive Discussion



## Abstract

Sea-salt aerosol mass, optical depth, and number concentration over the global oceans have significant implications for aerosol direct and indirect climate effects. We modeled sea-salt aerosol in a coupled climate and sectional microphysical model, CAM/CARMA, with aerosol dynamics including sea salt emission, gravitational sedimentation, dry deposition, wet scavenging, and particle swelling. We aimed at finding an integrated sea salt source function parameterization in the global climate model to simultaneously represent mass, optical depth, and number concentration. Each of these quantities is sensitive to a different part of the aerosol size distribution, which requires a size resolved microphysical model to treat properly. The CMS source function introduced in the research, based upon several earlier source functions, reproduced measurements of mass, optical depth and number concentration as well as the size distribution better than other source function choices we tried. However, as we note, it is also important to properly set the removal rate of the particles. The source function and removal rate are coupled in producing observed abundances. We find that sea-salt mass and optical depth peak in the winter, when winds are highest. However, surprisingly, particle numbers and CCN concentrations peak in summer when rainfall is lowest. The quadratic dependence of sea salt optical depth on wind speed, observed by some, is well represented in the model. We also found good agreement with the wind speed dependency of the number concentration at the measurement location and the regional scale. The work is the basis for further investigation of the effects of sea-salt aerosol on climate and atmospheric chemistry.

## 1 Introduction

Atmospheric sea salt aerosol (SSA) particles are produced by wind driven processes over the ocean and have sizes from tens of nanometers to several hundred microns. Since SSA does not have a large anthropogenic source it is usually treated as a back-

ACPD

10, 24499–24561, 2010

## Modeling sea-salt aerosol

T. Fan and O. B. Toon

Title Page

Abstract

Introduction

Conclusions

References

Tables

Figures

◀

▶

◀

▶

Back

Close

Full Screen / Esc

Printer-friendly Version

Interactive Discussion



ground aerosol. SSA dominates the particulate mass and is a major contributor to the aerosol optical depth over the remote ocean (Quinn et al., 1998). The scattering of sunlight by SSA particles modifies the radiation budget of the Earth system, which is known as “the aerosol direct effect”. SSA accounts for 50% of the local light scattering over the oceans and could contribute over a third of the column aerosol optical depth (Penner et al., 2001). The top-of-atmosphere clear sky global annual mean radiative forcing due to sea salt is estimated between  $-0.6$  and  $-5.03 \text{ Wm}^{-2}$  according to different models (Winter and Chylek, 1997; Haywood et al., 1999; Jacobson, 2001; Grini et al., 2002; Ayash et al., 2008; Ma et al., 2008). The region with the strongest direct radiative effect is the so-called “roaring forties” around  $40^\circ \text{S}$ . The large surface area concentration of SSA makes it the dominant scatterer over this region, not only for the supermicron (radius  $> 1 \mu\text{m}$ ) aerosol but also for the submicron aerosol (radius  $< 1 \mu\text{m}$ ) (Quinn et al., 1998; Bates et al., 2002).

Recent studies indicate the existence of many fine-mode and ultrafine-mode SSA particles that dominate the SSA number concentration (Clarke et al., 2006; Martensson et al., 2003). SSA particles activate as cloud condensation nuclei (CCN) and modify the cloud radiative properties and lifetimes, which is known as “the aerosol indirect effect”. SSA dominates the CCN over the remote ocean where wind speeds are high and/or other aerosol sources are weak (Murphy et al., 1998). They are more readily activated as CCN than sulfate aerosol due to their larger size and low supersaturation threshold (O’Dowd et al., 1999). The inclusion of SSA as small as  $0.01 \mu\text{m}$  increases CCN over the Southern Ocean by 150–500% relative to other CCN sources such as from sulfate (Pierce and Adams, 2006). In contrast, if the ultrafine particles are not considered, SSA contributes only 10% to cloud droplet number (Ayash et al., 2008). Moreover, SSA modulates the behavior of other aerosol species and gaseous precursors from both natural and anthropogenic sources. They provide surface area as a sink for the condensation of low-vapor-pressure gaseous species such as sulfuric and methanesulfonic acid so as to suppress the nucleation of new particles. Oxidation of  $\text{SO}_2$  is enhanced due to the higher pH associated with sea-salt droplets both inside

**Modeling sea-salt aerosol**

T. Fan and O. B. Toon

Title Page

Abstract

Introduction

Conclusions

References

Tables

Figures

◀

▶

◀

▶

Back

Close

Full Screen / Esc

Printer-friendly Version

Interactive Discussion



and outside the cloud (O'Dowd et al., 1997).

In conclusion, SSA affects the climate system by scattering solar radiation, modifying the properties of clouds in the marine boundary layer, and participating in heterogeneous chemistry. These effects are dominated by SSA burdens in different size ranges.

Therefore, uncertainties caused by errors in modeling the SSA production, transport and removal processes in any size range could lead to errors in climate forcing estimates.

In this study, we used a coupled climate-microphysical model to represent the dynamics and microphysical processes affecting SSA on a global scale. The goal of this paper is to test the model's capability to simulate three properties that are highly relevant to the direct and indirect climate effects of SSA: the mass of the aerosols, their optical depth and their number concentration. The results from three emission parameterizations of Gong (2003), Caffrey et al. (2006), and a combined Clarke et al. (2006), Monahan et al. (1986), and Smith et al. (1993) formulation (CMS hereinafter) will be compared. As we will discuss, the mass, the optical depth, and the number of SSA are controlled by distinctly different parts of the size distribution. The advantage of using a size-resolved microphysical model is that aerosol production, transport and removal are all calculated based on particle size. We can thus control the modeling of the physical processes and track the properties for each bin size, which adds more flexibility than in a model which does not resolve the size distribution. The following section describes the model setup. The results from the model, and comparisons with observations are given in Sect. 3. Section 4 provides a conclusion.

## 2 Model description

The microphysical model, which is based on the community aerosol and radiation model for atmospheres (CARMA, version 2.3) developed at the University of Colorado/National Aeronautics and Space Administration (NASA) (Toon et al., 1988), has been incorporated into the National Center for Atmospheric Research (NCAR)'s com-

## Modeling sea-salt aerosol

T. Fan and O. B. Toon

Title Page

Abstract

Introduction

Conclusions

References

Tables

Figures

◀

▶

◀

▶

Back

Close

Full Screen / Esc

Printer-friendly Version

Interactive Discussion



munity atmosphere model (CAM, version 3.1) (Collins et al., 2006) following the column physics interface algorithm. CARMA serves as a size-resolved aerosol microphysical component to replace CAM's bulk aerosol model. For the purpose of this investigation, the only aerosol species considered is sea salt. We used 16 sea salt mass bins to represent SSA. These mass bins correspond with dry radius bins logarithmically spaced between 0.01 and 15.2  $\mu\text{m}$ , including 10 submicron and 6 supermicron bins. Each size bin was treated by CAM as an individual advective tracer (Bardeen et al., 2008). We used 16 bins based on the results from test runs showing that mass concentrations using 16 size bins converge with those using 21 size bins.

We drove the model with 6-hourly National Center for Environmental Prediction (NCEP)/NCAR reanalysis fields for wind speed, temperature, surface water vapor flux and surface sensible heat flux. The meteorology input was linearly interpolated to a 30-min model time step. The horizontal grid spacing is  $2^\circ$  by  $2.5^\circ$ . There are 28 vertical layers. The bottom layer is approximately 120 m thick.

The aerosol processes considered include: (1) sea salt emission at the surface, (2) turbulent diffusion, (3) transport on a global scale, (4) gravitational sedimentation, (5) dry deposition at the surface, (6) scavenging by clouds and rain, and (7) particle growth by taking up water. The parameterizations used in each of these processes will be described in detail in the following sections. Coagulation is not considered in the model since the low number concentrations and short lifetime of SSA indicate that it is not an important process.

The particle sizes are tracked in the model by the dry mass of sea salt. Since wet particles smaller than 30  $\mu\text{m}$  (which will typically correspond to dry particles smaller than 15  $\mu\text{m}$ ) will evaporate to their ambient radius in a time period that is shorter than their lifetime (Fitzgerald et al., 1998; Lewis and Schwartz, 2004), it is assumed in our model that the particles reach equilibrium with the ambient environment instantaneously. The wet radii are calculated based on the model humidity at the time and location of interest as discussed below. Gravitational sedimentation, dry deposition, and optical properties take into account the wet radius of the SSA while turbulence and advective transport

## Modeling sea-salt aerosol

T. Fan and O. B. Toon

Title Page

Abstract

Introduction

Conclusions

References

Tables

Figures

◀

▶

◀

▶

Back

Close

Full Screen / Esc

Printer-friendly Version

Interactive Discussion



do not incorporate the wet radius, although there can be a significant humidity gradient coupled with rapid turbulent mixing (Caffrey et al., 2006).

Assumptions were made to compensate for the features that could not be captured due to the limited temporal and spatial resolution. Weibull wind speed distributions were adopted to represent the effect of wind gusts on SSA production, since the emission flux is a non-linear function of wind speed (Justus et al., 1978). Large particles have a short lifetime due to gravitational sedimentation, which is not well represented in a model with coarse vertical resolution. So we corrected the sea salt emission flux based on Hoppel et al. (2005), which mostly affects the large particles.

## 2.1 Emission

There are two major questions about the emission flux: what is the emission rate for different particle sizes and what is the dependence of emission rate on wind speed? The size-resolved SSA emission flux is also known as the source function. They are numerous proposed source functions based on in-situ measurements, laboratory experiments, or their combination. However, the uncertainty in SSA source functions is large due to difficulty in sampling over the ocean, limitation of the measurement equipment, scarcity of the data, the geographically varying nature of the sea salt emission, and the differing focuses of the researchers (Lewis and Schwartz, 2004). Our goal is to choose a source function that is suitable for global climate models and capable of representing the mass, optical depth, and number concentrations simultaneously.

Monahan et al. (1986) derived a source function by combining laboratory measurements of droplet number flux from bubbles per unit whitecap area and field measurements of whitecap coverage as a function of wind speed. Almost all source functions have followed their approach of using the whitecap area to determine the wind speed dependence of the fluxes.

Figure 1 shows the Monahan source function for particle number together with several other source functions. Several different physical effects are involved in SSA generation. Bursting bubbles in the foam from the whitecaps yield particles larger than

## Modeling sea-salt aerosol

T. Fan and O. B. Toon

Title Page

Abstract

Introduction

Conclusions

References

Tables

Figures

◀

▶

◀

▶

Back

Close

Full Screen / Esc

Printer-friendly Version

Interactive Discussion



about 1  $\mu\text{m}$  from small jets and particles smaller than 1  $\mu\text{m}$  from the film making up the bubble. Hence the origins of the particles differ across the size spectrum. The number fluxes for various source functions between 0.1 and 10  $\mu\text{m}$  are similar, except near 1  $\mu\text{m}$  where they differ by a factor of about 2. However, extrapolation of the Monahan source function to radii smaller than 0.1  $\mu\text{m}$  leads to very large particle production rates (Andreas, 1998; Vignati et al., 2001; Martensson et al., 2003). Gong (2003) suggested an extension of Monahan et al.'s source function that covers the size range as low as 0.01  $\mu\text{m}$ . However, Gong's submicron flux is low by many orders of magnitude compared with that from the laboratory measurements of Martensson et al. (2003), who developed their source function down to 0.01  $\mu\text{m}$  by measuring SSA in a bubble chamber using synthetic seawater. Clarke et al. (2006) later measured the SSA spectrum in a coastal zone with breaking waves and acquired the flux for the submicron particles, which is also orders of magnitude higher than Gong's submicron flux.

To simulate the SSA mass, optical depth and number, a source function that reasonably covers the whole size range is demanded. However, the applicable size ranges of the schemes mentioned above cut off at various lower or upper limits. For this reason, Caffrey et al. (2006) combined Clarke/Martensson, Monahan, and Smith et al. (1993) source functions. They took the larger of Monahan and Smith functions for radii from 0.15 to 15  $\mu\text{m}$  for wind speed above 9  $\text{m s}^{-1}$ , which is the threshold wind speed for spume droplets. Spume droplets are formed when the wind shears off wave crests. Studies are available for the production of spume droplets, though data are scarce (Burk, 1984; Stramska, 1987; Andreas, 1990; Smith et al., 1993). Reviews were given in Fitzgerald (1991) and Andreas et al. (1995). Smith et al. (1993) suggested a spume source function with an exponential function of radius and of wind speed up to 32  $\text{m s}^{-1}$ . Below 9  $\text{m s}^{-1}$ , they used the Monahan scheme alone. To make the Aitken-mode (radius < 0.1  $\mu\text{m}$ ) number more like Clarke or Martensson, Caffrey et al. (2006) extended the source function down to 0.01  $\mu\text{m}$  using the Monahan source function and multiplying the whole size range by a size-dependent factor  $W(r)$ , where  $r$  stands for dry particle radius.  $W(r)$  approaches 1 as the radius increases. However, as

## Modeling sea-salt aerosol

T. Fan and O. B. Toon

Title Page

Abstract

Introduction

Conclusions

References

Tables

Figures

◀

▶

◀

▶

Back

Close

Full Screen / Esc

Printer-friendly Version

Interactive Discussion





shown in Fig. 1, Caffrey et al. (2006)'s number flux is about one magnitude higher below  $0.1\ \mu\text{m}$  compared to Clarke et al. (2006). This order of magnitude difference in fluxes may reflect the wide range of fluxes found by Marttensson et al. (2003) depending on the temperature of the seawater.

Inspired by Caffrey et al. (2006), we introduced a combined Clarke, Monahan and Smith (CMS) source function as an alternative scheme. We directly adopted Clarke et al.'s source function below  $0.8\ \mu\text{m}$  and took the larger of the Monahan and the Smith function above  $0.8\ \mu\text{m}$ . Notice that we extended the Clarke source function to the  $0.1\text{--}1\ \mu\text{m}$  size range so that the CMS source function is larger in this mode than the Gong and the Caffrey source functions and comparable to Marttensson et al. (2003). We made this adjustment because, as we will see later, the Gong and the Caffrey schemes tend to underestimate the optical depth, which is dominated by particles between  $0.1\text{--}1\ \mu\text{m}$  in radius. We will compare results from Gong, Caffrey, and CMS source functions later in this paper and decide which one can best fit demands of this research. Their formulas and applicable size ranges are summarized in Table 1.

Many papers only display the source functions by number as in Fig. 1. However, many properties of the sea salt are relatively unrelated to the number of particles. In fact number, optical depth, and mass fluxes are each dominated by different size ranges of the source function. Of course, since large particles fall out rapidly, the injected mass at 10 m is dominated by larger sized particles than are found 60 m above the sea surface, where the mid-point of our first model layer typically occurs. From the perspective of climate modeling, a model that is only tested against sea salt mass is not guaranteed to properly represent optical depth or particle number.

Figure 2 shows the cross-sectional area and mass source functions at wind speeds of 5, 10, and  $20\ \text{m s}^{-1}$  at 10 m altitude for the Gong, Caffrey, and CMS source functions. As shown in Fig. 1 the number flux is controlled by particles smaller than  $0.1\ \mu\text{m}$ . Figure 2 shows that the area flux is dominated by particles with sizes near  $1\ \mu\text{m}$ , except that the contribution of very large particles becomes significant at high wind speed. The SSA area is usually related to the optical properties, such as the optical depth. The

## Modeling sea-salt aerosol

T. Fan and O. B. Toon

Title Page

Abstract

Introduction

Conclusions

References

Tables

Figures

◀

▶

◀

▶

Back

Close

Full Screen / Esc

Printer-friendly Version

Interactive Discussion





mass plots in Fig. 2, however, are dominated by particles with sizes near and above 10  $\mu\text{m}$ . We noticed that small slope changes of the Gong source function in the number plot of Fig. 1 translate into a mass peak at the end of the size ranges in Fig. 2. It is not clear in the development of the Gong source function whether the mass peak is meant to be realistic for bubble bursting, or to crudely represent spume particles. The Monahan formulation, which was the basis of the Gong formulation, was not meant to include generation of spume droplets. The Monahan source function does not show a mass peak above 10  $\mu\text{m}$  as in the Gong source function.

Generally the sea salt source function is designed to represent the flux at 10 m above the ocean surface. However, the mid-point of our model bottom layer is about 60 m. Hoppel et al. (2005) suggested applying a correction factor  $f_{\text{ref}}$  directly to the source function to account for the significant vertical gradient of large particles in the first model layer between 10 m and the layer mid-point:

$$f_{\text{ref}} = \left( \frac{\delta}{z_{\text{ref}}} \right)^{\frac{v_g}{\chi}} \quad (1)$$

Here  $\delta$  is the 10 m height where the source function is defined,  $z_{\text{ref}}$  is the reference height defined as the midpoint of model bottom layer, and  $v_g$  is the gravitational sedimentation velocity. The turbulence term is  $\chi = k u_*$ , where  $k$  is von Karman's constant,  $u_*$  is the friction velocity, which is obtained by  $u_* = C_D^{1/2} u_{10}$ , where

$$C_D = \begin{cases} 1.14 \times 10^{-3}, & u_{10} \leq 10 \text{ ms}^{-1} \\ (0.49 + 0.065 u_{10}) \times 10^{-3}, & u_{10} > 10 \text{ ms}^{-1} \end{cases} \quad (2)$$

$f_{\text{ref}}$  is close to 1 for small particles and decreases as particle size increases.  $u_{10}$  is the wind speed at 10 m. We multiplied the Caffrey and the CMS source functions, but not the Gong source function, by  $f_{\text{ref}}$ .

Here we assumed that aerosols were evenly mixed horizontally in a grid cell. Some grid cells are partly composed of land or sea ice. Therefore, the emission was multi-

## Modeling sea-salt aerosol

T. Fan and O. B. Toon

[Title Page](#)
[Abstract](#)
[Introduction](#)
[Conclusions](#)
[References](#)
[Tables](#)
[Figures](#)
[◀](#)
[▶](#)
[◀](#)
[▶](#)
[Back](#)
[Close](#)
[Full Screen / Esc](#)
[Printer-friendly Version](#)
[Interactive Discussion](#)


plied by the fraction of the open ocean area in these grids. Emission from leads within sea ice was not considered in our model.

## 2.2 Wind field

Among the environmental variables that influence the SSA production, wind speed is the major factor that controls the area of the whitecaps and hence the SSA fluxes. The lifting of sea salt, like the lifting of desert dust, depends on the power in the wind, and therefore varies approximately as the third power of the wind speed.

The wind field in CAM is taken from the 6-hourly NCEP/NCAR reanalysis I (Kalnay et al., 1996) and interpolated into 30-min time steps. The model runs in an offline mode which means that the wind field is forced back to interpolated NCEP wind speeds at the beginning of every time step. The wind dependence in the Monahan, Gong, Clarke, Caffrey, and CMS source functions is represented by a whitecap coverage function suggested by Monahan et al. (1986)

$$W_{\text{cap}}(u_{10}) = 3.84 \times 10^{-6} u_{10}^{3.41} \quad (3)$$

The 10 m wind was calculated from the wind speed from the model bottom layer assuming neutral atmospheric stability using the algorithm suggested by Large and Pond (1982). Note that we did not account for stability in deriving  $u_{10}$ , because the SSA should be a function of the friction velocity  $u_*$ . The whitecap observation were mostly taken under neutral atmospheric stability, so we can infer  $u_*$  from  $u_{10}$ . Hence the  $u_{10}$  we use is meant to be a pseudo  $u_{10}$  to compensate for the inappropriate use of  $u_{10}$  in the sea salt source functions, which instead should be cast in terms of  $u_*$ , as they are for dust lifting over land.

Since the grid cells of the global model are large and the emission rate grows as the cube of the wind speed, we adopted the Weibull wind speed distribution to represent the effect of wind gusts on production (Justus et al., 1978). To apply the probability

## Modeling sea-salt aerosol

T. Fan and O. B. Toon

Title Page

Abstract

Introduction

Conclusions

References

Tables

Figures

◀

▶

◀

▶

Back

Close

Full Screen / Esc

Printer-friendly Version

Interactive Discussion



distribution to the wind speed we rewrote the source function as

$$\frac{dF}{dr} = F(r) \int_{u_0}^{\infty} u^{3.41} p(u) du \quad (4)$$

Here the source function is divided into a size dependent part and a wind speed dependent part.  $F(r)$  depends on the source functions used, which are given in Table 1.

$u_0$  is the threshold wind speed below which there is no SSA production.  $u_0$  is taken to be  $4 \text{ m s}^{-1}$  in the model.  $u$  is the mean wind speed.  $p(u)$  is the a two-parameter Weibull distribution having the form

$$p(u) = \left(\frac{k}{c}\right) \left(\frac{u}{c}\right)^{k-1} \exp\left[-\left(\frac{u}{c}\right)^k\right] \quad (5)$$

with  $k$  as the shape parameter and  $c$  as the scale parameter. Following Grini and Zender (2004) for dust storms, we assume

$$k = 0.94 \sqrt{u} \quad (6)$$

$$c = u \left[ \Gamma(1 + 1/k) \right]^{-1} \quad (7)$$

in which  $\Gamma(a)$  is a gamma function defined by

$$\Gamma(a) = \int_0^{\infty} t^{a-1} e^{-t} dt \quad (8)$$

By solving the integral in Eq. (4), we have

$$\frac{dF}{dr} = F(r) c^{3.41} \Gamma\left(\frac{3.41}{k} + 1, \left(\frac{u_0}{c}\right)^k\right), \text{ or} \quad (9)$$

$$\frac{dF}{dr} = F(r) \left[ \frac{u}{\Gamma(1 + 1/k)} \right]^{3.41} \Gamma\left(\frac{3.41}{k} + 1, \left(\frac{u_0 \Gamma(1 + 1/k)}{u}\right)^k\right) \quad (10)$$

## Modeling sea-salt aerosol

T. Fan and O. B. Toon

Title Page

Abstract

Introduction

Conclusions

References

Tables

Figures

◀

▶

◀

▶

Back

Close

Full Screen / Esc

Printer-friendly Version

Interactive Discussion



in which  $\Gamma(a, x)$  is the incomplete gamma function defined by

$$\Gamma(a, x) = \int_x^{\infty} t^{a-1} e^{-t} dt \quad (11)$$

### 2.3 Gravitational sedimentation and dry deposition

The particles are moved down by gravitational sedimentation in each layer of the model, while the particles are removed by dry deposition in the bottom layer. Fall velocity,  $v_g$ , is first calculated for laminar flow using the formulas in Table 2. The second step is to obtain the Reynolds number,  $Re$ , which is calculated based on  $v_g$

$$Re = \frac{\text{Inertial force}}{\text{Viscous force}} = \frac{2\rho v_g r_p}{\mu} \quad (12)$$

Here  $r_p$  is the radius of the wet particle, calculated as in Sect. 2.4. If  $Re < 0.1$ , the flow is laminar and we accept  $v_g$  we just calculated. In practice  $v_g$  is usually in this limit except for the largest particles. If  $Re > 0.1$ , the flow is turbulent so that  $Re$  and  $v_g$  are recalculated.  $Re$  has been measured in the laboratory as a monotone function of  $C_D Re^2$ . We calculate  $C_D Re^2$  by

$$C_D Re^2 = \frac{32 r_p^3 \rho \rho_p g C_c}{3\mu} \quad (13)$$

The value of  $Re$  can be looked up in the  $Re - C_D Re^2$  relationship described in Pruppacher and Klett (1978). Associating the formula of  $v_g$  and  $Re$ , the gravitational sedimentation velocity is related to  $Re$  by

$$v_g = \frac{\mu Re}{2\rho r_p} \quad (14)$$

The definitions of the parameters in Eqs. (13) and (14) are given in Table 2. Examples of the gravitational sedimentation velocity are shown in Fig. 3.  $v_g$  varies a little with location since the wet radius depends on location.

Dry deposition of SSA particles refers to the transfer of SSA particles to the surface by gravitational sedimentation, turbulent transfer, Brownian diffusion, impaction, and interception by waves. It is reasonable to assume that the sea salt particles will not rebound at the ocean surface. The dry deposition flux  $f_d$  at a reference height is proportional to the mean number concentration  $n$

$$f_d = n \times v_d \quad (15)$$

where the constant of proportionality  $v_d$  is called the dry deposition velocity. In the model, the reference height is the midpoint of the bottom layer, consistent with the height of the concentration. We use the method described in Zhang et al. (2001)

$$v_d = v_g + \frac{1}{R_a + R_s} \quad (16)$$

Basically, the idea is to match the downward flux through the viscous sublayer with that through the surface layer. In the viscous sublayer, which is 0.1–1 mm thick above the surface, the SSA particles are mainly transported by Brownian diffusion, impaction and gravitational sedimentation. In the surface layer, which extends from above the viscous sublayer to the reference height, downward flux is dominated by turbulent diffusion and gravitational sedimentation. The transport of SSA particles is assumed to be retarded by the aerodynamic resistance,  $R_a$ , in the surface layer, and the surface resistance,  $R_s$ , in the viscous sublayer. The aerodynamic resistance is based on gradient-transport theory and the mass-transfer/momentum-transfer similarity.  $R_a$  depends on the atmospheric stability and surface roughness and is independent of aerosol species. The surface resistance of the viscous sublayer,  $R_s$  depends on particle size, atmospheric conditions and surface roughness. It is determined by Brownian diffusion, impaction, and interception, whose collection efficiencies are represented by  $E_B$ ,  $E_{IM}$ , and  $E_{IN}$ , respectively. The impaction is caused by the failure of an SSA particle to respond rapidly to non-uniform flow near the surface. Interception happens when the particle passes an obstacle at a distance shorter than its physical dimensions.

## Modeling sea-salt aerosol

T. Fan and O. B. Toon

Title Page

Abstract

Introduction

Conclusions

References

Tables

Figures

◀

▶

◀

▶

Back

Close

Full Screen / Esc

Printer-friendly Version

Interactive Discussion



In the model the deposition velocities for land, ocean and sea ice were treated separately. The aerodynamic resistance over land is calculated in the CAM land model with detailed land types. Over the ocean and ice we use the method introduced in Seinfeld and Pandis (1998) with roughness lengths of 0.0001 and 0.04 m, respectively. If the grid cell contains multiple surface types, the area fraction-weighted deposition velocity is used.

Figure 3 shows the dry deposition velocity over representative oceanic grid cells at wind speeds of  $5 \text{ m s}^{-1}$  and  $10 \text{ m s}^{-1}$ . Gravitational sedimentation dominates the removal of particles larger than  $20 \mu\text{m}$  in wet radius, while the surface resistance terms dominate the removal rate of small particles. The dry deposition is least efficient for particles between  $0.1$  and  $1 \mu\text{m}$  in radius. The velocities are larger at higher wind speeds, indicating a faster removal rate. Both the emission and dry deposition rates are larger at higher wind speeds.

The tendency of the constituent due to dry deposition can be calculated explicitly,

$$\frac{C^\tau - C^{\tau-1}}{\Delta\tau} = v_d \frac{C^\tau}{\Delta x} \quad (17)$$

in which  $C^\tau$  is concentration of a particular constituent, here SSA, at time  $\tau$ .  $\Delta\tau$  and  $\Delta x$  are time and space increments. In our model, to prevent negative concentrations of very large particles that can be caused by rapid removal in a model time step, we changed to the implicit method so that the concentrations decrease exponentially in time, i.e.,

$$\frac{C^{\tau+1} - C^\tau}{\Delta\tau} = v_d \frac{C^{\tau+1}}{\Delta x} \quad (18)$$

It should be noted that Eq. (18) is not the exact solution to the problem. However, it is equally as accurate as the explicit method and does not yield negative concentrations for large deposition velocities.

## Modeling sea-salt aerosol

T. Fan and O. B. Toon

Title Page

Abstract

Introduction

Conclusions

References

Tables

Figures

◀

▶

◀

▶

Back

Close

Full Screen / Esc

Printer-friendly Version

Interactive Discussion



## 2.4 Particle swelling

Sea salt particles take up water easily and grow in size. The particle swelling affects gravitational sedimentation and dry deposition due to the change of both particle size and density. The variation of dry deposition velocity between locations in Fig. 3 is due to the difference in particle swelling at different locations. It will also affect the optical depth calculation. The wet radius is calculated using a parameterization as a function of relative humidity (RH) by Gerber (1985),

$$r_w = \left[ \frac{C_1 r_d^{C_2}}{C_3 r_d^{C_4} - \log RH} + r_d^3 \right]^{1/3} \quad (19)$$

where  $C_1 = 0.7674$ ,  $C_2 = 3.079$ ,  $C_3 = 2.573 \times 10^{-11}$ , and  $C_4 = -1.424$ .  $r_w$  and  $r_d$  are the wet and dry radius in cm. The relative humidity values used in this expression were for the middle of our model layers. Figure 4 shows the ratio of wet radius to dry radius at different relative humidity values. Noting that Gerber's formula cannot be extrapolated to near- or super-saturated conditions, we limit the surface relative humidity to be less than 98% when we calculate the wet radius. The theoretical base for this choice is that the mole fraction of water in seawater of salinity 35‰ is very close to 0.98. The vapor pressure of water in equilibrium with a seawater droplet is therefore expected to be 98% of the vapor pressure of water at the same temperature.

The wet density,  $\rho_w$ , is calculated by

$$\rho_w = \left( \rho r_d^3 + \rho_{H_2O} (r_w^3 - r_d^3) \right) / r_w^3 \quad (20)$$

Here  $\rho$  is the density of dry sea salt having a value of  $2.17 \text{ g cm}^{-3}$ .

## 2.5 Wet scavenging

We utilized the wet scavenging procedure for aerosol in CAM, which accounts for both in-cloud and below-cloud scavenging. The below-cloud scavenging, or washout, fol-

## Modeling sea-salt aerosol

T. Fan and O. B. Toon

Title Page

Abstract

Introduction

Conclusions

References

Tables

Figures

◀

▶

◀

▶

Back

Close

Full Screen / Esc

Printer-friendly Version

Interactive Discussion





lows Dana and Hales (1976) and Balkanski et al. (1993), assuming that both rain and snow remove aerosol below the cloud. The mixing ratio loss rate by below-cloud scavenging,  $L_{W,bc}$ , is calculated by

$$L_{W,bc} = \frac{\Lambda}{P} P q \quad (21)$$

where  $\frac{\Lambda}{P}$  is the washout coefficient,  $\Lambda$ , normalized to unit rainfall rate,  $P$ . The default washout coefficient in CAM wet scavenging scheme is  $0.1 \text{ mm}^{-1}$ .  $P$  is precipitation in  $\text{mm h}^{-1}$ , which could be rain or snow.  $q$  is the aerosol mass mixing ratio.

The CAM default in-cloud scavenging assumes that 100% of the SSA particles reside in the cloud water and are later removed with the fraction of cloud water that is converted to rain. This percentage is called the solubility factor, ranging from 0 to 1, which also decides the percentage of aerosol dissolved in rain or snow droplets, so it affects both below-cloud and in-cloud scavenging. It is further assumed that the aerosol in the rain can be released back to the atmosphere if the rain droplet evaporates.

The wet scavenging rate in CAM is tied to cloud parameterizations including the cloud fraction, cloud water, and production rate of precipitation, etc. It has been noticed that CAM among many other global models produces more persistence rainfall than observed (Deng et al., 2007), which leads to overestimated wet scavenging. We are aware of a bug in the wet scavenging code that has recently been found in CAM3.1 and its later versions. However, reasonable lifetimes can still be obtained by tuning the parameters, i.e., the solubility factor.

We adjusted the solubility factor in our model by determining the wet scavenging lifetime. In an idealized case where only emission and wet scavenging is turned on, the tendency of the concentration  $C$  ( $\text{kg m}^{-2}$ ) is calculated as  $\frac{\partial C}{\partial t} = S - L_{\text{wet}} C$ , where  $S$  is the emission rate ( $\text{kg m}^{-2} \text{ s}^{-1}$ ), and  $L_{\text{wet}}$  is the loss rate due to wet scavenging ( $\text{s}^{-1}$ ). When equilibrium is reached ( $\frac{\partial C}{\partial t} = 0$ ),  $L_{\text{wet}} = \frac{S}{C} = 1/\tau_{\text{wet}}$ . Here  $\tau_{\text{wet}}$  is the wet scavenging residence time (s). Figure 5 shows the variations of the global-averaged residence time and loss rate with the solubility factor at equilibrium. The mean wet scavenging

## Modeling sea-salt aerosol

T. Fan and O. B. Toon

Title Page

Abstract

Introduction

Conclusions

References

Tables

Figures

◀

▶

◀

▶

Back

Close

Full Screen / Esc

Printer-friendly Version

Interactive Discussion



rate for sea salt reported in 12 models is  $0.79 \text{ day}^{-1}$ , equivalent to a residence time of 1.26 day (Textor et al., 2006). The corresponding solubility is 0.55. However, the lifetime varied considerably between models. Therefore, we used solubility factors of 0.3, 0.5, and 0.8 in our model simulations.

### 3 Results

#### 3.1 Mass concentration

We compared the modeled mass concentration with the measurements at eight coastal sites from the University of Miami global network (Savoie and Prospero, 1977). Since the CMS and the Caffrey source function are similar in the large particle range, we only compared the CMS and the Gong source functions. We also tested three solubility factors of 0.3, 0.5, and 0.8. The measurements were mostly obtained on a daily or weekly basis. To align the model results to the measurements in the same time frame, we carried out seven-day averages of the model results for the same days as in the measurements. Daily or weekly data, depending on the data output frequency, that are more than one standard deviation from the yearly mean were eliminated from the comparison. This approach may eliminate storms or measurement errors.

The slopes and the correlation coefficients of the linear fits between measurements and model results are shown in Table 3. The agreements for mass of both source functions are only weakly dependent on the solubility factor, which is not surprising since the sink for the large particles that dominate the mass has a significant component due to sedimentation. The correlations do equally well when the solubility factor is equal to 0.5 as the other values. However, as we will show below, the correlation and slope are better for the optical depth when we choose a solubility factor of 0.5. The model using CMS source function and the solubility factor of 0.5 captures the seasonal variation at the eight coastal sites very well as shown in Fig. 6. The scatter plot between measurements and model results at the eight sites is also given in Fig. 6. The slope of scatter

### Modeling sea-salt aerosol

T. Fan and O. B. Toon

Title Page

Abstract

Introduction

Conclusions

References

Tables

Figures

◀

▶

◀

▶

Back

Close

Full Screen / Esc

Printer-friendly Version

Interactive Discussion



plot is 0.93 and the correlation is 0.47.

The CMS source function includes the spume droplet production at wind speed higher than  $9 \text{ ms}^{-1}$  while the Gong source function does not produce spume at high wind speed. It is not realistic for the Gong source function to have high emission rates for particles larger than  $1 \mu\text{m}$  at low wind speed as shown in Fig. 2b. Likewise, neglect of spume causes the Gong source function to predict lower emission than CMS source function at high wind speeds. Note that we did not apply the Hoppel correction to the Gong source function that could make even lower emission for the large particles at high wind speeds. Therefore, although the Gong source function gives comparable results to the CMS, we consider CMS to be more realistic as a function of wind speed.

The CMS source function includes the Hoppel et al. (2005) large particle gradient correction. The total global averaged mass concentration using the Hoppel correction is decreased by 14.6% compared to that without the Hoppel correction. The correction for gradients of large particles in thick model layers near the surface influences the prediction of mass concentration and should be considered in models with low vertical resolution.

SSA mass concentration over continents is a good indicator of the removal processes since there is no SSA production over land. Figure 7 shows the fine-mode SSA mass concentration over the United States in 2006 compared with the IMPROVE (Interagency Monitoring of Protected Visual Environments) dataset. The loss rate for fine-mode particles should be dominated by washout and rainout. The IMPROVE data measures the chloride ion over more than 200 sites in the United States. To obtain the sea salt mass the chloride concentration is multiplied by 1.8 to represent the sodium ions, which are not analyzed by IMPROVE. Underestimation of IMPROVE sea salt mass results from chlorine depletion in the reaction of SSA with gaseous nitrate acid (DeBell et al., 2006). The minimum/maximum SSA mass concentrations are  $0.014/2.18 \mu\text{g m}^{-3}$  for the IMPROVE data and  $0.018/4.89 \mu\text{g m}^{-3}$  for the model. Model results are higher (mainly at coastal sites) but comparable to the IMPROVE data, which indicates the model has reasonable removal mechanisms. The low horizontal resolu-

## Modeling sea-salt aerosol

T. Fan and O. B. Toon

Title Page

Abstract

Introduction

Conclusions

References

Tables

Figures

◀

▶

◀

▶

Back

Close

Full Screen / Esc

Printer-friendly Version

Interactive Discussion



tion of the model ( $2^\circ \times 2.5^\circ$ ) may be a factor in some of the disagreement between the model and data.

### 3.2 Optical depth

The aerosol optical depth,  $\tau$ , is the vertically integrated aerosol extinction from the bottom to the top of atmosphere. It is calculated in the model as

$$\tau = \int_z \int_{r_w} \pi r_w^2 \frac{dN(r_w, z)}{dr_w} q_{\text{ext}} dr_w dz \quad (22)$$

where  $\frac{dN(r_w, z)}{dr_w}$  is the size-resolved number concentration as a function of the wet radius,  $r_w$ , and altitude,  $z$ .  $q_{\text{ext}}$  is the efficiency factor for extinction, which is the ratio between extinction area and geometric area.  $q_{\text{ext}}$  is a function of wavelength, which is calculated by the Mie code in CARMA. The value of  $q_{\text{ext}}$  asymptotes to 2 when the particles are several times larger than the wavelength of light. Since SSA particles in the oceanic environment are mainly made up of water, we utilize the refractive index of water when computing the efficiency factor for extinction. By integrating over all the particle sizes and all the vertical levels, we obtained the aerosol optical depth for the whole column. Note that the optical depth is proportional to the square of the wet radius so it is very sensitive to particle swelling with ambient relative humidity.

#### 3.2.1 Comparison with AERONET optical depth

It is not easy to match the modeled sea salt optical depth to the optical depth measurement either from ground or from space, since the measured optical depth contains the impact from all the aerosol species. Sea salt seldom dominates the marine optical depth. Therefore, to compare our model optical depth with AERONET (AERosol RObotic NETwork) retrievals, we chose Midway Island in the middle of the Pacific Ocean that is away from dust storm tracks, biomass-burning smoke plumes, and anthropogenic pollution sources. Smirnov et al. (2003) stated Midway as the only

AERONET site where he could clearly separate the sea salt optical depth. We compared the model with the coarse-mode optical depth to lessen the impact of small particles that are likely not sea salt. To further exclude the seasonal impacts from other aerosol sources, we eliminated the data points when the instantaneous optical depths are over 0.3.

Figure 8 is the monthly-averaged model and AERONET optical depth using Gong, Caffrey, and CMS source functions for 2006. Note that mass data as in Fig. 6 is not available for 2006, so we could not compare mass and optical depth for the same year. Here we averaged the daytime model output when AERONET retrievals are available. The mean squared error (MSE) between the model and AERONET are  $1.68 \times 10^{-3}$ ,  $1.52 \times 10^{-3}$ , and  $6.25 \times 10^{-4}$  for Gong, Caffrey, and CMS source functions, respectively, so CMS source function gives the best fit. As we can see from the source function in Fig. 2, the elevated 0.1–1  $\mu\text{m}$  size range of the CMS source function leads to higher optical depth and better fit to the AERONET retrievals.

### 3.2.2 Relationship between optical depth and wind speed

Madry et al. (2010) have shown that a useful constraint on SSA optical depth can be obtained from its wind speed dependence. A correlation between wind speed and sea salt optical depth has been suggested by many researchers (Hoppel et al., 1990; Smirnov et al., 2003; Satheesh et al., 2006; Mulcahy et al., 2008). However, considerable scatter about this correlation may remain due to pollution in the boundary layer and free-troposphere/stratosphere aerosols contributing to optical depth. Evident correlation can be obtained only when stable atmospheric conditions are being experienced and uniform clean marine air masses are being studied. A power-law relationship

$$\tau_{\lambda=500\text{nm}} = 0.06 + 0.00055 \cdot U^{2.195} \quad (23)$$

with a high correlation ( $r^2 = 0.97$ ) was found for wind speed up to  $18 \text{ m s}^{-1}$  at Mace Head, Ireland (Mulcahy et al., 2008). The analysis was carried out under stable wind conditions and very stringent criteria for selecting the clean marine air mass. To ensure

## Modeling sea-salt aerosol

T. Fan and O. B. Toon

Title Page

Abstract

Introduction

Conclusions

References

Tables

Figures

◀

▶

◀

▶

Back

Close

Full Screen / Esc

Printer-friendly Version

Interactive Discussion



that the measured optical depth properties are representative of the corresponding wind speed conditions, Mulcahy et al. (2008) filtered their samples by “stable wind condition”, which required daily standard deviation of wind speed less than  $2 \text{ m s}^{-1}$  and standard deviation during optical depth measurements less than  $1 \text{ m s}^{-1}$ . Only 14 days out of 10 months of data is left for analyzing the optical depth–wind speed dependence. Other datasets show similar dependence over a wide area (Smirnov et al., 2003; Satheesh et al., 2006). Madry et al. (2010) found that a sea salt model produced similar wind speed dependence over the global ocean.

Our model wind field is the 6-hourly NCEP reanalysis wind fields linearly interpolated to a 30-min time step and therefore the high-frequency variation of wind speed is smoothed out. Therefore we defined the “stable wind condition” by requiring the daily standard deviation of the wind speed be less than  $1 \text{ m s}^{-1}$ . On average about 35% of the model days are filtered out. The constant term in optical depth–wind speed dependence of Mulcahy et al. (2008) reflects the wind-independent optical depth component, which includes the contribution of residual sea salt and the free-troposphere/stratosphere aerosols. Our model results indicate that the optical depth under windless condition (the constant term) with sea salt only is less than Mulcahy et al.’s 0.06. The power-law optical depth–wind speed dependence is well reproduced by our model by scaling Mulcahy et al.’s constant term down from 0.06 to 0.02. Table 3 shows that the global sea salt optical depths are well reproduced by the CMS source function and the solubility factor of 0.5. The Gong source function underestimates the optical depths even with low solubility factor of 0.3.

Figure 9 shows the modeled optical depth at wavelength of 500 nm as a function of wind speed in the North Atlantic and the “roaring forties”. Optical depths in the “roaring forties” grow with wind speed more rapidly at high wind conditions in our model than in the formulation based on Mulcahy et al.’s coefficients. Table 4 shows the power-law fits of the modeled optical depth–wind speed dependence in five oceanic regions. The low MSE of the fitting function show that the modeled optical depths are well represented by the quadratic power-law relationship. The correlations between the calculated optical

## Modeling sea-salt aerosol

T. Fan and O. B. Toon

Title Page

Abstract

Introduction

Conclusions

References

Tables

Figures

◀

▶

◀

▶

Back

Close

Full Screen / Esc

Printer-friendly Version

Interactive Discussion



depth from Mulcahy et al.'s relationship and the model are as high as 0.99. Although the power-law relationship is applicable in all the regions, differences can be found in the coefficients. The exponent is generally larger than the 2.195 value in Mulcahy et al.'s relationship when derived from our model, indicating stronger enhancement of optical depth with increased wind speed in the model. Figure 10 shows the scatter plot comparing latitudinal-averaged optical depth from the model and calculated from Mulcahy et al.'s formula from 70° S to 70° N. The slope of 0.97 and correlation of 0.93 indicates the model and the function derived from the measurements agree very well over the global oceans. Similar high correlations were found by Madry et al. (2010). Note that the variability in the modeled optical depths denoted by the error bars are so large that the differences in the power laws from Mulcahy et al. (2008) and our model are not significant.

### 3.3 Number concentration

Unfortunately, it is even more difficult to find data on sea salt number concentration than on optical depth. Most condensation nuclei (CN) and cloud condensation nuclei (CCN) data do not distinguish aerosol composition. In addition, there are no data from a network on CN and CCN, as there are for optical depth and mass. Many researchers have carried out investigations on the wind speed dependence of marine aerosol number concentration as reviewed by Lewis and Schwartz (2004). Only a few of them discriminated SSA from other marine aerosols using the thermal heating technique (O'Dowd and Smith, 1993; Shinozuka et al., 2004).

The wind speed dependence is typically expressed by a log-linear relationship

$$\log N = a_N U_{10} + N_0 \quad (24)$$

We compare our model results with the ship measurements over the Northeast Atlantic (63° N, 8° W) by O'Dowd and Smith (1993) in October 1989 down to radius as small as 0.05 μm in Fig. 11. The data covers wind speeds as high as 17 m s<sup>-1</sup>. Here we interpolated the model size ranges to the four size ranges of the measurement. The model

## Modeling sea-salt aerosol

T. Fan and O. B. Toon

Title Page

Abstract

Introduction

Conclusions

References

Tables

Figures

◀

▶

◀

▶

Back

Close

Full Screen / Esc

Printer-friendly Version

Interactive Discussion





results generally agree with the measurements in all four size ranges. However, the model produced higher concentrations for the particles with radius of 0.05–0.1  $\mu\text{m}$  than observed. We conclude from the comparison between model and the measurement that the reasonable range of  $a_N$  coefficients varies from 0.08 to 0.10 for radius smaller than 1.5  $\mu\text{m}$  for the measurement location.

We also compared our model with the First Aerosol Characterization Experiment (ACE-1) dataset. We averaged the model concentration over the ACE-1 campaign region in the Southwest Pacific (40–56° S, 135–160° E) and compared with ACE-1 data (Shinozuka et al., 2004) in Fig. 12. Also included in Fig. 12 are the data obtained by O'Dowd and Smith (1993). We use their data instead of the regression fit because we would have higher number concentration at high wind speeds using their regression function than the actual data. The ACE-1 data are for submicron size ranges (0.075–0.5  $\mu\text{m}$ ) and the O'Dowd and Smith (1993) data are for size ranges 0.05–0.15  $\mu\text{m}$ , and 0.19–0.42  $\mu\text{m}$ . The model size range is interpolated to be as consistent as possible with the measurement data (0.075–0.15  $\mu\text{m}$ , 0.19–0.42  $\mu\text{m}$ ). Both measurements show a near-zero offset while the model offset, which was set to zero in Fig. 12 for comparison, was about  $10\text{ cm}^{-3}$ . The different offset between the model and the data could be due to the slower rainout rate in the model, which brings more SSA from the upwind direction. Again, the model and the data are in different years, which could also bring in some of the discrepancies. To focus on the dependency on wind speeds, we scale down the model and measurement values in Fig. 12 by subtracting the lowest values in the corresponding datasets. The regression fit to the model results generally agrees with the measurements although numbers are higher than the measurements at moderate wind speeds ( $7\text{--}13\text{ m s}^{-1}$ ). We explored whether the model overestimate could be caused by the rainfall evaporation scheme, which releases particles back at their original size when raindrops evaporate. In reality aerosols should merge inside drops to form larger particles. We find model number concentrations are reduced by about 8.6% if we let the small particles grow into larger ones after rain droplets evaporate, which is not enough to explain the overestimation.

## Modeling sea-salt aerosol

T. Fan and O. B. Toon

Title Page

Abstract

Introduction

Conclusions

References

Tables

Figures

◀

▶

◀

▶

Back

Close

Full Screen / Esc

Printer-friendly Version

Interactive Discussion



At wind speeds above  $13 \text{ m s}^{-1}$  the model number concentration falls below the regression line in Fig. 12. Figure 13 illustrates the modeled wind speed dependence of the emission flux compared with the eddy covariance measurements of sea spray particle emission by Norris et al. (2008). The data were fitted to a log-linear relationship between the fluxes and the wind speed. The model emission flux is a power-law relationship with the wind speed so the shape is different than the data, but we still give the log-linear fits in the figure. Smaller slopes for the model were found for particles with radius of  $0.15 \mu\text{m}$  as well as other size ranges not shown here. The model produces less SSA particles than from the relationship derived from the measurement at high wind speeds. Therefore, it is possible that some mechanism that could increase the production rate at high wind speed is not included in the existing source functions.

### 3.4 Size distribution

#### 3.4.1 Comparison with AERONET size distribution

Particle size distributions for radius from  $0.05$  to  $15 \mu\text{m}$  were retrieved by AERONET using a flexible inversion algorithm developed by Dubovik and King (2000). Figure 14a demonstrates the AERONET-derived and model-produced volumetric size distribution under ambient relative humidity at Midway Island in March, June, and September 2006. AERONET size distributions are retrieved in actual (wet) particle radius. Therefore, we also display the model results in wet radius. Particles with the same dry radius could grow into different wet sizes because of the different relative humidity values in different vertical layers. To facilitate combining the functions in various vertical layers, we defined a set of “universal wet radius bins”, which extends to  $82.7 \mu\text{m}$ . We first calculated the wet radius at each layer for each of our original dry salt bins. Then we redistributed the particles to the “universal wet radius bins” in such a way that both the dry mass and the number are conserved in the splitting.

AERONET reports volume size distribution in their data products. However, the light scattering mainly depends on the cross-sectional area of the particles. Hence we

## Modeling sea-salt aerosol

T. Fan and O. B. Toon

Title Page

Abstract

Introduction

Conclusions

References

Tables

Figures

◀

▶

◀

▶

Back

Close

Full Screen / Esc

Printer-friendly Version

Interactive Discussion



believe the data are actually more reliable for area distribution. Therefore, we converted the AERONET volumetric size distribution,  $dV/d\ln r$ , to the area size distribution,  $dA/d\ln r$ , by

$$\frac{dA}{d\ln r} = \frac{3}{4r} \frac{dV}{d\ln r} \quad (25)$$

5 where  $A$  is the cross-sectional area. The results are shown in Fig. 14b. We normalized the model volumetric and area size distribution so that the total volume and cross-sectional area are the same for the model and AERONET for particles larger than  $0.44 \mu\text{m}$ . We did not normalize to the whole size range since AERONET shows a significant mode near  $0.1 \mu\text{m}$ . This mode is probably due to sulfate and organic aerosols from the oceans or pollution aerosols that are not represented in the model.

10 The modeled size distribution basically reflects the coarse mode in the AERONET bi-modal size distribution inversion. The model volumetric size distributions show two modes, one near  $3 \mu\text{m}$  and the other near  $30 \mu\text{m}$ . Clearly a significant amount of volume is in the very large mode, which comes from spume generation. The data do not show the presence of the spume mode probably because AERONET retrievals are not sensitive to volume but to area. The model spans to larger sizes, but is questionable because the spume droplet generation is hard to observe and may be poorly represented in the model. The large particles may not instantaneously grow to equilibrium state with ambient relative humidity as we assumed in the model. The spume mode contributes little to the area of the particles. The shape of the modeled area size distribution basically matches the coarse-mode AERONET size distribution, though there are variations from month to month.

### 3.4.2 Comparison with in-situ measurement

25 Since it is not possible to determine the number concentration of SSA in the AERONET retrievals, we compared our modeled size distribution with in-situ measurements at the surface. Figure 15 shows the modeled number size distributions using Gong, Caf-

## Modeling sea-salt aerosol

T. Fan and O. B. Toon

Title Page

Abstract

Introduction

Conclusions

References

Tables

Figures

◀

▶

◀

▶

Back

Close

Full Screen / Esc

Printer-friendly Version

Interactive Discussion



frey, and CMS source functions. Comparison was made to the observation during the NEAT'89 cruise in Northeast Atlantic (O'Dowd et al., 1997). A tri-modal log-normal function was fitted to the measurements for film, jet, and spume droplet modes,

$$\frac{dN}{d\log r} = \sum_{i=1,3} \frac{N_i}{\ln \sigma_i \sqrt{2\pi}} e^{-\frac{(\ln(r) - \ln(r_{mi}))^2}{2\ln^2 \sigma_i}} \quad (26)$$

5  $i = 1, 2, 3$  for film, jet and spume, where  $N_i$  is the total number concentration for that mode,  $r_{mi}$  is the mode radius and  $\sigma_i$  is the standard deviation.

$$\log N_1 = 0.095U_{10} + 0.283, \quad r_{m1} = 0.1 \mu\text{m}, \quad \sigma_1 = 1.9 \quad (27)$$

$$\log N_2 = 0.0422U_{10} - 0.288, \quad r_{m2} = 1 \mu\text{m}, \quad \sigma_2 = 2 \quad (28)$$

$$\log N_3 = 0.069U_{10} - 3.5, \quad r_{m3} = 6 \mu\text{m}, \quad \sigma_3 = 3 \quad (29)$$

10 We corrected the wet radius given by the measurement data to dry radius. We applied the correction of the equations given by Vigniti et al. (2001). The applicable range of the data is 0.05–15  $\mu\text{m}$  of dry radius.

Also shown in Fig. 15 is the canonical distribution from Lewis and Schwartz (2004), which is an empirical relationship that is based on 21 measurements of size distributions of SSA concentrations over the global oceans (refer to Table 13 in Lewis and Schwartz, 2004), which includes the measurement of O'Dowd et al. (1997). The canonical size distribution is

$$\frac{dN}{d\log_{10} r_{80}} = n_0 e^{\left\{ -\frac{1}{2} \left[ \frac{\ln(r_{80}/r_{80}')}{\ln \sigma} \right]^2 \right\}} \quad (30)$$

20 where  $n_0 = 0.07U_{10}^2$ ,  $r_{80}$  is the radius at relative humidity of 80%,  $r_{80}' = 0.3 \mu\text{m}$  is the geometric mean radius, and  $\sigma = 2.8$  is the geometric standard deviation. Here we use the model 10 m wind speed for the functions suggested by O'Dowd et al. (1997)

## Modeling sea-salt aerosol

T. Fan and O. B. Toon

Title Page

Abstract

Introduction

Conclusions

References

Tables

Figures

◀

▶

◀

▶

Back

Close

Full Screen / Esc

Printer-friendly Version

Interactive Discussion



and Lewis and Schwartz (2004). Since the measurements were taken under various conditions that may introduce uncertainties, we normalize the size distribution so that only the shape of the size distribution is the major concern here. The normalization criteria is that the cross sectional area for particles larger than  $0.07\text{ }\mu\text{m}$  is the same for all the model results and the measurements.

Figure 15 shows that the model number concentration in the coarse mode ( $1\text{--}15\text{ }\mu\text{m}$ ) from the three source functions matches the measurements very well. The differences are trivial considering the small magnitude of the concentration (less than  $1\text{ cm}^{-3}$ ). The model number concentrations of the three source functions in the  $0.1\text{--}1\text{ }\mu\text{m}$  size range have very similar shapes and also match the canonical size distribution in the  $0.5\text{--}1\text{ }\mu\text{m}$  size range. The function of O'Dowd et al. (1997) is lower than the model results in the  $0.5\text{--}1\text{ }\mu\text{m}$  size range, which could be due to the gap between two-modes in the fitting function. The major difference between the three source functions comes from particles in the size range  $0.01\text{--}0.1\text{ }\mu\text{m}$  that dominate the number concentration. However, very few measurements in this size range are incorporated in the canonical size distribution.

A recent study that extends down to ultra-fine SSA particles examined the thermal stability and growth factor of the marine aerosol particles in a wide range of sizes (Clarke et al., 2006). Figure 16 shows that the percentages of particles smaller than a certain particle radius using the CMS source function agrees with the measurement of Clarke et al. (2006). Note that we have converted the diameter range of  $0.01\text{--}8\text{ }\mu\text{m}$  in Clarke et al.'s figure to the radius range of  $0.01\text{--}4\text{ }\mu\text{m}$ . 54.8% of sea salt particles are smaller than  $0.05\text{ }\mu\text{m}$  in dry radius in Clarke et al.'s data. We list the number concentration and the fraction of the particles smaller than  $0.05\text{ }\mu\text{m}$  from our model and the canonical size distribution by Lewis and Schwartz (2004) in Table 5. The Gong source function gives about 10% of sea salt number coming from particles smaller than  $0.05\text{ }\mu\text{m}$ , which is close to the canonical size distribution but much lower than 54.8% as observed. The Caffrey and CMS source functions give a much larger fraction of around 85% and 60% of particles smaller than  $0.05\text{ }\mu\text{m}$ , because they are based on Clarke et al. (2006),

## Modeling sea-salt aerosol

T. Fan and O. B. Toon

Title Page

Abstract

Introduction

Conclusions

References

Tables

Figures

◀

▶

◀

▶

Back

Close

Full Screen / Esc

Printer-friendly Version

Interactive Discussion



which indicates the existence of large amount of ultra-fine SSA particles. CMS gives the closest estimate for the fraction of particles smaller than  $0.05\text{ }\mu\text{m}$ . Gong's source function rejected the small particles in the Monahan source function (see Fig. 1).

Figure 17 shows the mass and cross-sectional area size distribution compared with that inferred from the Lewis and Schwartz (2004) canonical size distribution. They are normalized so that the cross-sectional area for particles larger than  $0.07\text{ }\mu\text{m}$  is the same for all the model results and the measurements. The mass and the cross-sectional area distribution in the coarse mode match the canonical size distribution very well for the Gong and Caffrey source functions. The CMS source function gives a lower coarse mode because of the normalization since the CMS cross-sectional area below  $1\text{ }\mu\text{m}$  is higher than the other two. We should notice that the higher value in the  $0.1\text{--}1\text{ }\mu\text{m}$  size range of CMS source function leads to a better agreement in the optical depth versus wind speed estimation in the relationship by Mulcahy et al. (2008). All source functions for mass produce results which agree with the canonical one in the radius range from  $0.1$  to  $1\text{ }\mu\text{m}$ . The differences in the mass and cross-sectional area below  $0.1\text{ }\mu\text{m}$  are not important for the integrated mass and area due to their small magnitude.

Figure 18 shows the percentages of modeled number, cross-sectional area, and mass concentration smaller than a certain particle radius using the CMS source function. We demonstrate in Fig. 18 that number, area, and mass are dominated by different particles sizes. The radius at which the number, area, and mass concentration reaches 50% of the total is  $0.055\text{ }\mu\text{m}$ ,  $1\text{ }\mu\text{m}$ , and  $3.7\text{ }\mu\text{m}$ , respectively.

### 3.5 SSA global distribution

Figure 19 shows the global distribution of optical depth using the CMS source function in the boreal winter and summer of 2006. The optical depths are usually high ( $>0.1$ ) in the roaring forties ( $40\text{--}60^\circ\text{S}$ ) in the Southern Hemisphere where the wind blows fiercely all through the year. The optical depths are also relatively large in the high-latitude oceans of the Northern Hemisphere in winter when the wind strengthens. The optical depths are low in the tropical region in both seasons due to the low wind speeds.

## Modeling sea-salt aerosol

T. Fan and O. B. Toon

Title Page

Abstract

Introduction

Conclusions

References

Tables

Figures

◀

▶

◀

▶

Back

Close

Full Screen / Esc

Printer-friendly Version

Interactive Discussion



The optical depth increases in the summer monsoon season over the Indian Ocean. Basically the optical depth distribution follows the wind speed pattern. Tropical rainfall could also contribute to low optical depth by removing of SSA particles. The high optical depths near Peru are due to the effect of the Andes Mountains on the NCEP wind field.

Figure 20 shows the global distribution of number concentration in the surface layer in the size range of 0.01–15  $\mu\text{m}$  in the boreal winter and summer of 2006. The concentration is typically about 10–50  $\text{cm}^{-3}$ , but can be over 150  $\text{cm}^{-3}$  in the “roaring forties”. Persistent high concentrations exist in the “roaring forties” in the two seasons. Low values can be seen in the tropics and again high concentration in the summer monsoon season over India Ocean. However, the seasonal variation of number concentrations does not correspond with that of the wind speed or optical depth. Although it is true for every season that the number concentration increases with wind speed, the increases are different among seasons. For example referring to Fig. 19 the optical depth is highest over the North Pacific, North Atlantic and roaring forties in the winter for the hemisphere in question, while the number density is highest in summer.

The different seasonal patterns of optical depth and number concentration are likely due to the different removal mechanisms in different particle size ranges. Figure 21 shows the loss rate of particles as a function of radius for 30–60° N and 30–60° S in boreal summer and winter. Dry deposition, wet scavenging and total loss rate are shown in Fig. 21. The loss rates were calculated by dividing the global removal flux by the global concentration (Balkanski et al., 1993). In both seasons and hemispheres wet scavenging is the dominant process removing particles smaller than about 1  $\mu\text{m}$ . Therefore, the number concentration is influenced by wet scavenging as well as wind speed which controls the production rate. Although the emission in the Northern Hemisphere during boreal winter is higher than in summer, precipitation removes SSA particles more effectively in winter so the number concentration in Northern Hemisphere increase from winter to summer. In contrast to the situation for small particles, the optical depth is most influenced by particles larger than 1  $\mu\text{m}$ . Dry deposition is important

**Modeling sea-salt aerosol**

T. Fan and O. B. Toon

Title Page

Abstract

Introduction

Conclusions

References

Tables

Figures

◀

▶

◀

▶

Back

Close

Full Screen / Esc

Printer-friendly Version

Interactive Discussion





for particles larger than 1  $\mu\text{m}$  in both winter and summer. Dry deposition depends only weakly on wind speed, and not at all on rainfall. Therefore, the optical depth pattern follows the wind speed because the emission as a function of wind speed controls the concentration.

5 Figure 22 illustrates the CCN number concentration at a supersaturation of 0.1%, which is a subset of number concentration with radius larger than 0.07  $\mu\text{m}$ . Typically sea salt could contribute 10–20  $\text{cm}^{-3}$  to the CCN in the tropics and as much as 80  $\text{cm}^{-3}$  to the CCN in the “roaring forties”. In the model there is a CNN “hot spot” near Peru, which is an artifact because of the wind field. CCN follow the same seasonal pattern as  
10 the extra-tropical number concentration being highest in summer when there are fewer rainfall events.

## 4 Conclusions

We developed a SSA model based on a coupled climate and microphysical model CAM/CARMA with detailed aerosol dynamical processes. A combined CMS source  
15 function, inspired by Caffrey et al. (2006), that incorporates different source functions from the literature in various size ranges into one source function, has been compared with other traditional source functions. Mass, optical depth, and number concentration are well modeled. The advantages of the CMS source function in modeling mass, optical depth, number concentrations, as well as the size distribution are illustrated in  
20 Table 3 and Fig. 16.

While the focus in the literature has generally been on source functions, we find that removal processes are equally important. We adjusted the wet scavenging rate in our model so that the corresponding residence time is consistent with the AEROCOM estimation. We find that SSA mass and optical depth peak in the winter, when winds  
25 are highest. However, surprisingly, particle numbers and CCN concentrations peak in summer when rainfall is lowest. This difference in seasonal behavior is due to the fact that the particles controlling mass and optical depth have significant removal rates due

## Modeling sea-salt aerosol

T. Fan and O. B. Toon

Title Page

Abstract

Introduction

Conclusions

References

Tables

Figures

◀

▶

◀

▶

Back

Close

Full Screen / Esc

Printer-friendly Version

Interactive Discussion



to sedimentation, while the small particles that control number are lost by rainout and washout.

Although data, which are now becoming old, exist for sea salt mass, there are relatively few datasets for optical depth and number concentration that are specific to sea salt. One way to isolate sea salt is through wind speed relationships. However, data seem particularly lacking for SSA less than  $0.1\ \mu\text{m}$  and for larger spume droplets. Based on available measurements, the model reproduced the wind-dependence of the SSA optical depth measured by Mulcahy et al. (2008) in Ireland, though we also noticed that the modeled dependence varied slightly among different oceans. The “roaring forties” tends to have larger optical depth at higher wind speed in the model than suggested from the Mulcahy formulation.

We found good agreement between the model and the wind speed dependence of the number concentration found at one measurement location. The wind dependence was also well reproduced by the model on a regional scale when compared to multiple datasets. However, the model over predicted the zero wind speed number concentrations. We did not model the same years when the data were obtained, so this difference in zero wind speed concentrations may reflect different rainfall amounts between the modeled year and the observed year. The fraction of particles smaller than  $0.05\ \mu\text{m}$  modeled by the CMS source function agreed well with measurements. The model estimated a CCN concentration of about  $10\text{--}20\ \text{cm}^{-3}$  in the tropics and as high as  $80\ \text{cm}^{-3}$  in the “roaring forties”.

The modeled SSA particle size distribution agreed well with the AERONET coarse-mode area size distributions. We do not think AERONET size distribution inversion products are suitable for sea salt volume.

This work is the basis for future studies we plan of marine aerosol direct and indirect effects using the coupled CAM/CARMA model.

*Acknowledgements.* We thank William Madry for helpful discussions about this work, and Charles Bardeen for help meshing CARMA and CAM. The work was supported by NSF grant ATM-0856007.

## Modeling sea-salt aerosol

T. Fan and O. B. Toon

Title Page

Abstract

Introduction

Conclusions

References

Tables

Figures

◀

▶

◀

▶

Back

Close

Full Screen / Esc

Printer-friendly Version

Interactive Discussion



## References

- Andreas, E. L.: Model estimates of the effects of sea spray on air-sea heat fluxes, Mar. Sci. Inst., Univ. of Conn., Avery Point Groton, 17–28, 1990.
- Andreas, E. L., Edson, J. B., Monahan, E. C., Rouault, M. P., and Smith, S. D.: The spray contribution to net evaporation from the sea – a review of recent progress, Bound.-Lay. Meteorol., 72, 3–52, 1995.
- Andreas, E. L.: A new sea spray generation function for wind speeds up to  $32 \text{ m s}^{-1}$ , J. Phys. Oceanogr., 28, 2175–2184, 1998.
- Ayash, T., Gong, S., and Jia, C. Q.: Direct and indirect shortwave radiative effects of sea salt aerosols, J. Climate, 21, 3207–3220, doi:10.1175/2007jcli2063.1, 2008.
- Balkanski, Y. J., Jacob, D. J., Gardner, G. M., Graustein, W. C., and Turekian, K. K.: Transport and residence times of tropospheric aerosols inferred from a global 3-dimensional simulation of Pb-210, J. Geophys. Res., 98, 20573–20586, 1993.
- Bardeen, C. G., Toon, O. B., Jensen, E. J., Marsh, D. R., and Harvey, V. L.: Numerical simulations of the three-dimensional distribution of meteoric dust in the mesosphere and upper stratosphere, J. Geophys. Res., 113, D17202, doi:10.1029/2007jd009515, 2008.
- Bates, T. S., Coffman, D. J., Covert, D. S., and Quinn, P. K.: Regional marine boundary layer aerosol size distributions in the Indian, Atlantic, and Pacific Oceans: a comparison of INDOEX measurements with ACE-1, ACE-2, and Aerosols99, J. Geophys. Res., 107(19), 8026, doi:10.1029/2001jd001174, 2002.
- Burk, S. D.: The generation, turbulent transfer and deposition of the sea-salt aerosol, J. Atmos. Sci., 41, 3040–3049, 1984.
- Caffrey, P. F., Hoppel, W. A., and Shi, J. J.: A one-dimensional sectional aerosol model integrated with mesoscale meteorological data to study marine boundary layer aerosol dynamics, J. Geophys. Res., 111, D24201, doi:10.1029/2006jd007237, 2006.
- Clarke, A. D., Owens, S. R., and Zhou, J. C.: An ultrafine sea-salt flux from breaking waves: implications for cloud condensation nuclei in the remote marine atmosphere, J. Geophys. Res., 111, D06202, doi:10.1029/2005jd006565, 2006.
- Collins, W. D., Rasch, P. J., Boville, B. A., Hack, J. J., McCaa, J. R., Williamson, D. L., Briegleb, B. P., Bitz, C. M., Lin, S. J., and Zhang, M. H.: The formulation and atmospheric simulation of the community atmosphere model version 3 (CAM3), J. Climate, 19, 2144–2161, 2006.

## Modeling sea-salt aerosol

T. Fan and O. B. Toon

Title Page

Abstract

Introduction

Conclusions

References

Tables

Figures

◀

▶

◀

▶

Back

Close

Full Screen / Esc

Printer-friendly Version

Interactive Discussion



- Dana, M. T. and Hales, J. M.: Statistical aspects of washout of polydisperse aerosols, *Atmos. Environ.*, 10, 45–50, 1976.
- DeBell, L. J., Gebhart, K. A., Hand, J. L., Malm, W. C., Pitchford, M. L., Schichtel, B. A., and White, W. H.: Spatial and seasonal patterns and temporal variability of haze and its constituents in the United States Report IV, Cooperative Institute for Research in the Atmosphere, USA, 217–218, 2006.
- Deng, Y., Bowman, K. P., and Jackson, C.: Differences in rain rate intensities between TRMM observations and community atmosphere model simulations, *Geophys. Res. Lett.*, 34, L01808, doi:10.1029/2006gl027246, 2007.
- Dubovik, O. and King, M. D.: A flexible inversion algorithm for retrieval of aerosol optical properties from Sun and sky radiance measurements, *J. Geophys. Res.*, 105, 20673–20696, 2000.
- Fitzgerald, J. W.: Marine aerosols – a review, *Atmos. Environ.*, 25, 533–545, 1991.
- Fitzgerald, J. W., Hoppel, W. A., and Gelbard, F.: A one-dimensional sectional model to simulate multicomponent aerosol dynamics in the marine boundary layer – 1. Model description, *J. Geophys. Res.*, 103, 16085–16102, 1998.
- Gerber, H. E.: Relative-Humidity Parameterization of the Navy Aerosol Model (NAM), Naval Research Laboratory, Washington, DC, 1985.
- Gong, S. L.: A parameterization of sea-salt aerosol source function for sub- and super-micron particles, *Global Biogeochem. Cy.*, 17, 1097, doi:10.1029/2003gb002079, 2003.
- Grini, A., Myhre, G., Sundet, J. K., and Isaksen, I. S. A.: Modeling the annual cycle of sea salt in the global 3D model Oslo CTM2: concentrations, fluxes, and radiative impact, *J. Climate*, 15, 1717–1730, 2002.
- Grini, A. and Zender, C. S.: Roles of saltation, sandblasting, and wind speed variability on mineral dust aerosol size distribution during the Puerto Rican Dust Experiment (PRIDE), *J. Geophys. Res.*, 109, D07202, doi:10.1029/2003jd004233, 2004.
- Haywood, J. M., Ramaswamy, V., and Soden, B. J.: Tropospheric aerosol climate forcing in clear-sky satellite observations over the oceans, *Science*, 283, 1299–1303, 1999.
- Hoppel, W. A., Fitzgerald, J. W., Frick, G. M., Larson, R. E., and Mack, E. J.: Aerosol size distributions and optical-properties found in the marine boundary-layer over the Atlantic-Ocean, *J. Geophys. Res.*, 95, 3659–3686, 1990.
- Hoppel, W. A., Caffrey, P. F., and Frick, G. M.: Particle deposition on water: surface source versus upwind source, *J. Geophys. Res.*, 110, D10206, doi:10.1029/2004jd005148, 2005.

## Modeling sea-salt aerosol

T. Fan and O. B. Toon

Title Page

Abstract

Introduction

Conclusions

References

Tables

Figures

◀

▶

◀

▶

Back

Close

Full Screen / Esc

Printer-friendly Version

Interactive Discussion



## Modeling sea-salt aerosol

T. Fan and O. B. Toon

Title Page

Abstract

Introduction

Conclusions

References

Tables

Figures

◀

▶

◀

▶

Back

Close

Full Screen / Esc

Printer-friendly Version

Interactive Discussion



- Jacobson, M. Z.: Global direct radiative forcing due to multicomponent anthropogenic and natural aerosols, *J. Geophys. Res.*, 106, 1551–1568, 2001.
- Justus, C. G., Hargraves, W. R., Mikhail, A., and Graber D.: Methods for estimating wind speed frequency distribution, *J. Appl. Meteorol.*, 17, 350–353, 1978.
- 5 Kalnay, E., Kanamitsu, M., Kistler, R., Collins, W., Deaven, D., Gandin, L., Iredell, M., Saha, S., White, G., Woollen, J., Zhu, Y., Chelliah, M., Ebisuzaki, W., Higgins, W., Janowiak, J., Mo, K. C., Ropelewski, C., Wang, J., Leetmaa, A., Reynolds, R., Jenne, R., and Joseph, D.: The NCEP/NCAR 40-year reanalysis project, *B. Am. Meteorol. Soc.*, 77, 437–471, 1996.
- Large, W. G. and Pond, S.: Sensible and latent-heat flux measurements over the Ocean, *J. Phys. Oceanogr.*, 12, 464–482, 1982.
- 10 Lewis, E. R. and Schwartz, S. E.: Sea salt aerosol production. Mechanisms, methods, measurements, and models, American Geophysical Union, Washington, DC, USA, 2004.
- Ma, X., von Salzen, K., and Li, J.: Modelling sea salt aerosol and its direct and indirect effects on climate, *Atmos. Chem. Phys.*, 8, 1311–1327, doi:10.5194/acp-8-1311-2008, 2008.
- 15 Madry, W. L., Toon, O. B., and O'Dowd, C. D.: Modeled optical thickness of the sea salt aerosol over the world ocean, 2006, *J. Geophys. Res.*, doi:10.1029/2010JD014691, under review, 2010.
- Martensson, E. M., Nilsson, E. D., de Leeuw, G., Cohen, L. H., and Hansson, H. C.: Laboratory simulations and parameterization of the primary marine aerosol production, *J. Geophys. Res.*, 108, 4297, doi:10.1029/2002jd002263, 2003.
- 20 Monahan, E. C., Spiel, D. E., and Davidson, K. L.: A model of marine aerosol generation via whitecaps and wave disruption, in: *Oceanic Whitecaps and their Role in Air-sea Exchange Processes*, edited by: MacNiocaill, E. C. M. G., Reidel, Dordrecht, The Netherlands, 167–174, 1986.
- 25 Mulcahy, J. P., O'Dowd, C. D., Jennings, S. G., and Ceburnis, D.: Significant enhancement of aerosol optical depth in marine air under high wind conditions, *Geophys. Res. Lett.*, 35, L16810, doi:10.1029/2008gl034303, 2008.
- Murphy, D. M., Anderson, J. R., Quinn, P. K., McInnes, L. M., Brechtel, F. J., Kreidenweis, S. M., Middlebrook, A. M., Posfai, M., Thomson, D. S., and Buseck, P. R.: Influence of sea-salt on aerosol radiative properties in the Southern Ocean marine boundary layer, *Nature*, 392, 62–65, 1998.
- 30 Norris, S. J., Brooks, I. M., de Leeuw, G., Smith, M. H., Moerman, M., and Lingard, J. J. N.: Eddy covariance measurements of sea spray particles over the Atlantic Ocean, *Atmos. Chem.*

- Phys., 8, 555–563, doi:10.5194/acp-8-555-2008, 2008.
- O'Dowd, C. D. and Smith, M. H.: Physicochemical properties of aerosols over the Northeast Atlantic – evidence for wind-speed-related submicron sea-salt aerosol production, *J. Geophys. Res.*, 98, 1137–1149, 1993.
- 5 O'Dowd, C. D., Smith, M. H., Consterdine, I. E., and Lowe, J. A.: Marine aerosol, sea-salt, and the marine sulphur cycle: a short review, *Atmos. Environ.*, 31, 73–80, 1997.
- O'Dowd, C. D., Lowe, J. A., and Smith, M. H.: Coupling sea-salt and sulphate interactions and its impact on cloud droplet concentration predictions, *Geophys. Res. Lett.*, 26, 1311–1314, 1999.
- 10 Penner, J. E., Andreae, M., Annegarn, H., Barrie, L., Feichter, J., Hegg, D., Jayaraman, A., Leaitch, R., Murphy, D., Nganga, J., Pitari, G., et al.: Aerosols, their direct and indirect effects, in: *Climate Change 2001: The Scientific Basis, Contribution of Working Group I to the Third Assessment Report of the Intergovernmental Panel on Climate Change*, edited by: Houghton, J. T., Cambridge University Press, 289–348, 2001.
- 15 Pierce, J. R. and Adams, P. J.: Global evaluation of CCN formation by direct emission of sea salt and growth of ultrafine sea salt, *J. Geophys. Res.*, 111, D06203, doi:10.1029/2005jd006186, 2006.
- Pruppacher, H. R. and Klett, J. D.: *Microphysics of Clouds and Precipitation*, Kluwer Academic, Dordrecht, The Netherlands, 1978.
- 20 Quinn, P. K., Coffman, D. J., Kapustin, V. N., Bates, T. S., and Covert, D. S.: Aerosol optical properties in the marine boundary layer during the first aerosol characterization experiment (ACE1) and the underlying chemical and physical aerosol properties, *J. Geophys. Res.*, 103, 16547–16563, 1998.
- Satheesh, S. K., Srinivasan, J., and Moorthy, K. K.: Contribution of sea-salt to aerosol optical depth over the Arabian Sea derived from MODIS observations, *Geophys. Res. Lett.*, 33, L03809, doi:10.1029/2005gl024856, 2006.
- 25 Savoie, D. L. and Prospero, J. M.: Aerosol concentration statistics for Northern Tropical Atlantic, *J. Geophys. Res.*, 82, 5954–5964, 1977.
- Seinfeld, J. H. and Pandis, S. N.: *Atmospheric Chemistry and Physics: From Air Pollution to Climate Change*, 2nd ed., Wiley, Hoboken, 1998.
- 30 Shinozuka, Y., Clarke, A. D., Howell, S. G., Kapustin, V. N., and Huebert, B. J.: Sea-salt vertical profiles over the Southern and Tropical Pacific Oceans: microphysics, optical properties, spatial variability, and variations with wind speed, *J. Geophys. Res.*, 109, D24201,

## Modeling sea-salt aerosol

T. Fan and O. B. Toon

Title Page

Abstract

Introduction

Conclusions

References

Tables

Figures

◀

▶

◀

▶

Back

Close

Full Screen / Esc

Printer-friendly Version

Interactive Discussion



doi:10.1029/2004jd004975, 2004.

Smirnov, A., Holben, B. N., Eck, T. F., Dubovik, O., and Slutsker, I.: Effect of wind speed on columnar aerosol optical properties at Midway Island, *J. Geophys. Res.*, 108, 4802, doi:10.1029/2003jd003879, 2003.

5 Smith, M. H., Park, P. M., and Consterdine, I. E.: Marine aerosol concentrations and estimated fluxes over the sea, *Q. J. Roy. Meteor. Soc.*, 119, 809–824, 1993.

Stramska, M.: Vertical profiles of sea salt aerosol in the atmospheric surface layer: a numerical model, *Acta. Geophys. Polonica*, 35, 87–100, 1987.

10 Textor, C., Schulz, M., Guibert, S., Kinne, S., Balkanski, Y., Bauer, S., Berntsen, T., Berglen, T., Boucher, O., Chin, M., Dentener, F., Diehl, T., Easter, R., Feichter, H., Fillmore, D., Ghan, S., Ginoux, P., Gong, S., Grini, A., Hendricks, J., Horowitz, L., Huang, P., Isaksen, I., Iversen, I., Kloster, S., Koch, D., Kirkevåg, A., Kristjansson, J. E., Krol, M., Lauer, A., Lamarque, J. F., Liu, X., Montanaro, V., Myhre, G., Penner, J., Pitari, G., Reddy, S., Seland, Ø., Stier, P., Takemura, T., and Tie, X.: Analysis and quantification of the diversities of aerosol life cycles within AeroCom, *Atmos. Chem. Phys.*, 6, 1777–1813, doi:10.5194/acp-6-1777-2006, 2006.

15 Toon, O. B., Turco, R. P., Westphal, D., Malone, R., and Liu, M. S.: A multidimensional model for aerosols – description of computational analogs, *J. Atmos. Sci.*, 45, 2123–2143, 1988.

Vignati, E., de Leeuw, G., and Berkowicz, R.: Modeling coastal aerosol transport and effects of surf-produced aerosols on processes in the marine atmospheric boundary layer, *J. Geophys. Res.*, 106, 20225–20238, 2001.

20 Winter, B. and Chylek, P.: Contribution of sea salt aerosol to the planetary clear-sky albedo, *Tellus B*, 49, 72–79, 1997.

Zhang, L. M., Gong, S. L., Padro, J., and Barrie, L.: A size-segregated particle dry deposition scheme for an atmospheric aerosol module, *Atmos. Environ.*, 35, 549–560, 2001.

25

ACPD

10, 24499–24561, 2010

## Modeling sea-salt aerosol

T. Fan and O. B. Toon

Title Page

Abstract

Introduction

Conclusions

References

Tables

Figures

◀

▶

◀

▶

Back

Close

Full Screen / Esc

Printer-friendly Version

Interactive Discussion





# Modeling sea-salt aerosol

T. Fan and O. B. Toon

Title Page

Abstract

Introduction

Conclusions

References

Tables

Figures

◀

▶

◀

▶

Back

Close

Full Screen / Esc

Printer-friendly Version

Interactive Discussion



**Table 1.** Formulas for source functions compared in the paper, unit:  $\text{m}^{-2} \text{s}^{-1} \mu\text{m}^{-1}$ .

Source Function	Formula	Size Range
Gong (2003)	$(dF/dr)_{\text{Gong}} = 1.373u_{10}^{3.41}r^{-A} \left(1 + 0.057r^{3.45}\right) \times 10^{1.607e^{-B^2}} *$ $A = 4.7(1 + \Theta)r^{-0.017r^{-1.44}}, \quad \Theta = \text{adjustable parameter} = 30,$ $B = (0.433 - \log r)/0.433$	0.01–15 $\mu\text{m}$
Caffrey et al. (2006)	$(dF/dr)_{\text{Monahan}} = 1.373u_{10}^{3.41}r^{-3}(1 + 0.057r^{1.05}) \times 10^{1.19e^{-B^2}}$ $B = (0.38 - \log r)/0.65$ $(dF/dr)_{\text{Caffrey}} = (dF/dr)_{\text{Monahan}} \times W(r)$ $W(r) = 1.136^{-r^{-0.855}} \left(1 + \frac{0.2}{r}\right)$	0.01–0.15 $\mu\text{m}$
	$(dF/dr)_{\text{Caffrey}} = \begin{cases} u_{10} < 9 \text{ ms}^{-1}, (dF/dr)_{\text{Monahan}} \\ u_{10} > 9 \text{ ms}^{-1}, \max((dF/dr)_{\text{Monahan}}, (dF/dr)_{\text{Smith}}) \end{cases}$ $\times W(r),$ where $(dF/dr)_{\text{Smith}} = \sum_{i=1}^2 A_i \exp\left\{-f_i [\ln(r_{80}/r_i)]^2\right\}, **$ $f_1 = 3.1, f_2 = 3.3, r_1 = 2.1 \mu\text{m}, r_2 = 9.2 \mu\text{m}$ $\log(A_1) = 0.0676u_{14} + 2.43*, \quad \log(A_2) = 0.959u_{14} - 1.476$	0.15–15 $\mu\text{m}$
CMS Fan and Toon (2010)	$(dF/dr)_{\text{CMS}} = (dF/dr)_{\text{Clarke}} = (dF/dr)_{\text{BW}} \cdot W_{\text{cap}}(u_{10})$ $(dF/dr)_{\text{BW}} = \sum_{i=1}^3 A_i$ $A_i = \beta_0 + \beta_1 D + \beta_2 D^2 + \beta_3 D^3 + \beta_4 D^4 + \beta_5 D^5,$ $D = \text{diameter} = 2r.$ See Table 1 in (Clarke et al., 2006) for $\beta$ coefficients, The whitecap coverage $W_{\text{cap}}(u_{10}) = 3.84 \times 10^{-6} u_{10}^{3.41}$ same as Caffrey et al. (2006) in size range of 0.15–15 $\mu\text{m}$	0.01–0.8 $\mu\text{m}$
		0.8–15 $\mu\text{m}$

\*  $u_{10}$  and  $u_{14}$  is the wind speed at 10 m and 14 m, respectively.

\*\*  $r$  is the dry radius,  $r_{80}$  is the radius at 80% relative humidity.

**Table 2.** Dry deposition scheme.

Item	Formula	Parameter settings
Gravitational sedimentation velocity	$v_g = \frac{2}{9} \frac{r_p^2 \rho_p g C_c}{\mu}, \text{ laminar}$ $v_g = \frac{\mu R e}{2 \rho_p r_p}, \text{ turbulent}$	$r_p$ =wet particle radius, $\rho_p$ =wet particle density, $g$ =gravitational acceleration $\mu$ =dynamic viscosity of air= $1.7 \times 10^{-5}$ , $C_c$ =slip correction factor $= 1 + \frac{\lambda}{r_p} \left[ 1.257 + 0.4 \exp \left( -\frac{1.1 r_p}{\lambda} \right) \right]$ , $\lambda$ =mean free path of air fluid.
Aerodynamic resistance	Ocean/sea ice $R_a = \frac{\ln(z_r/z_o) - \psi_H}{\kappa u_*}$ Land from CAM land model	$z_r$ =center of bottom layer, $z_o$ =roughness length= 0.0001 (ocean), 0.04 (sea ice), $\kappa$ =Von Karman constant= 0.4, $\psi_H$ =stability function. $u_*$ =friction velocity
Surface layer resistance	$R_s = \frac{1}{\varepsilon_0 u_* (E_B + E_{IM} + E_{IN}) R_1}$	$R_1$ =fraction of particles that stick to the surface= 1 $\varepsilon_0^*$ =empirical constant= 1
Brownian diffusion efficiency	$E_B = S c^{-\gamma}$	$S c$ =Schmidt Number= $v_a / D_B$ , $v_a$ =kinetic air viscosity $D_B$ =Brownian diffusivity= $\frac{kT}{6\pi\rho_a v_a r} C_c$ , $k$ =Boltzmann constant, $T$ =temperature, $\rho_a$ =air density. $\gamma = 1/2$ for water surface
Impaction efficiency	$E_{IM} = 10^{-3/St}$	Stokes number= $\frac{v_g u_*^2}{g v_a}$
Interception efficiency	$E_{IN} = 0$	Neglected in this research

\*  $\varepsilon_0 = 3$  in Zhang et al. (2001). Since it is an empirical constant, we choose 1 in our simulation.

# Modeling sea-salt aerosol

T. Fan and O. B. Toon

**Table 3.** Slopes ( $S$ ) and Correlations ( $R$ ) of the linear fits of the in-situ measurements and model.

Source function	Solubility factor	Mass Model= $S_M$ SP	Optical Depth Model= $S_r$ Mulcahy
Gong	0.3	$S_M = 1.10, R = 0.54$	$S_r = 0.73, R = 0.95$
Gong	0.5	$S_M = 0.97, R = 0.51$	$S_r = 0.55, R = 0.93$
Gong	0.8	$S_M = 0.86, R = 0.46$	$S_r = 0.42, R = 0.92$
CMS	0.3	$S_M = 1.09, R = 0.51$	$S_r = 1.33, R = 0.94$
CMS	0.5	$S_M = 0.93, R = 0.47$	$S_r = 0.97, R = 0.93$
CMS	0.8	$S_M = 0.80, R = 0.42$	$S_r = 0.73, R = 0.91$

SP: global network of aerosol measurements (Savoie and Prospero, 1977).

Mulcahy: wind speed dependence of sea salt optical depth (Mulcahy et al., 2008).

[Title Page](#)
[Abstract](#)
[Introduction](#)
[Conclusions](#)
[References](#)
[Tables](#)
[Figures](#)
[I◀](#)
[▶I](#)
[◀](#)
[▶](#)
[Back](#)
[Close](#)
[Full Screen / Esc](#)
[Printer-friendly Version](#)
[Interactive Discussion](#)


## Modeling sea-salt aerosol

T. Fan and O. B. Toon

**Table 4.** Aerosol optical depth ( $\tau$ )-wind speed ( $u_{10}$ ) dependence of the fitting function in global oceanic regions.

Region	Coordinate		Optical depth-wind speed	MSE	$R$	%Stable wind
N. Atlantic	EQ–60 N	75 W–180 W	$\tau = 0.030 + 0.00022u_{10}^{2.499}$	$5.84 \times 10^{-5}$	0.9967	72.8%
S. Atlantic	60 S–EQ	75 W–20 E	$\tau = 0.026 + 0.00063u_{10}^{2.143}$	$1.19 \times 10^{-4}$	0.9961	62.0%
N. Pacific	EQ–60 N	145 E–120 W	$\tau = 0.037 + 0.00001u_{10}^{2.767}$	$9.56 \times 10^{-5}$	0.9944	73.4%
S. Pacific	60 S–EQ	150 E–75 W	$\tau = 0.036 + 0.00001u_{10}^{3.007}$	$1.23 \times 10^{-4}$	0.9898	72.4%
Indian Ocean	60 S–30 N	20 E–145 E	$\tau = 0.017 + 0.00041u_{10}^{2.374}$	$2.44 \times 10^{-5}$	0.9990	70.5%
Roaring Forties	60 S–40 S	0 E–0 W	$\tau = 0.042 + 0.00017u_{10}^{2.659}$	$1.38 \times 10^{-5}$	0.9967	45.2%
Southern Ocean	65 S–60 S	0 E–0 W	$\tau = 0.043 + 0.00080u_{10}^{2.899}$	$1.10 \times 10^{-4}$	0.9911	49.9%

MSE: mean square error.  $R$ : Correlation.

[Title Page](#)
[Abstract](#)
[Introduction](#)
[Conclusions](#)
[References](#)
[Tables](#)
[Figures](#)
[I◀](#)
[▶I](#)
[◀](#)
[▶](#)
[Back](#)
[Close](#)
[Full Screen / Esc](#)
[Printer-friendly Version](#)
[Interactive Discussion](#)


**Modeling sea-salt aerosol**

T. Fan and O. B. Toon

**Table 5.** Monthly-averaged number concentration and fraction of particles with radius of 0.01–0.05  $\mu\text{m}$  at Midway Island in June 2006.

Source functions/data	Number concentration ( $\text{cm}^{-3}$ )	Fraction
Gong	1.5	9.4%
Caffrey	96.3	82.4%
CMS	47.5	58.7%
Clarke et al. (2006)	N/A	54.8%
Lewis and Schwartz (2004)	0.45	10.1%

Title Page

Abstract

Introduction

Conclusions

References

Tables

Figures

I◀

▶I

◀

▶

Back

Close

Full Screen / Esc

Printer-friendly Version

Interactive Discussion



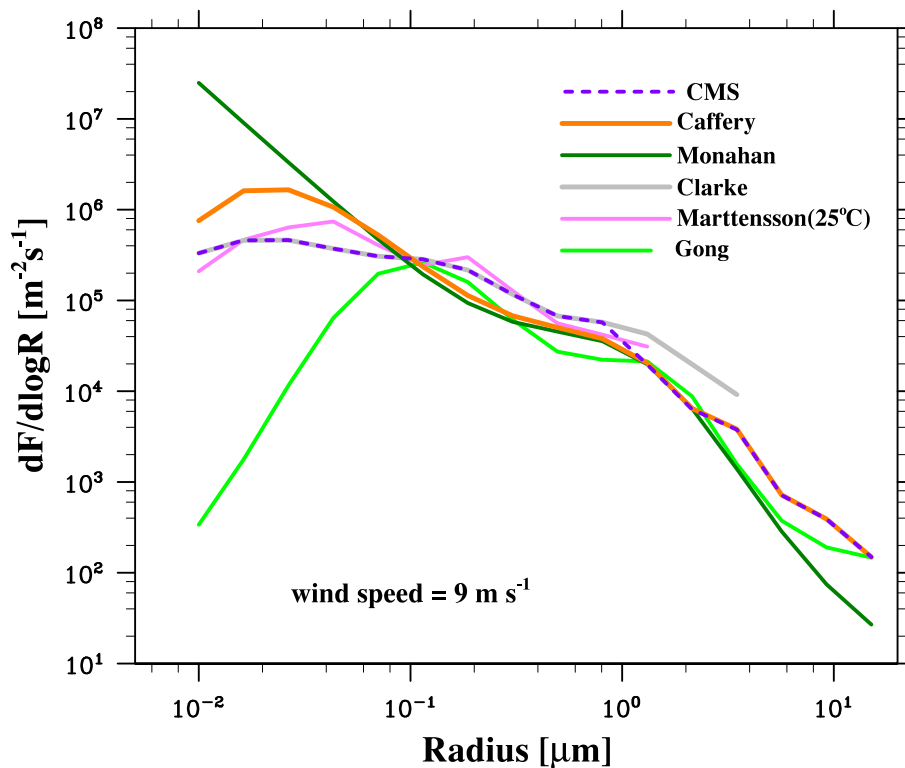


**Fig. 1.** The number fluxes from several sea salt source functions. All of the source functions except for Gong are corrected for gravitational sedimentation following Hoppel et al. (2005).

## Modeling sea-salt aerosol

T. Fan and O. B. Toon

Title Page

Abstract

Introduction

Conclusions

References

Tables

Figures

◀

▶

◀

▶

Back

Close

Full Screen / Esc

Printer-friendly Version

Interactive Discussion



## Modeling sea-salt aerosol

T. Fan and O. B. Toon

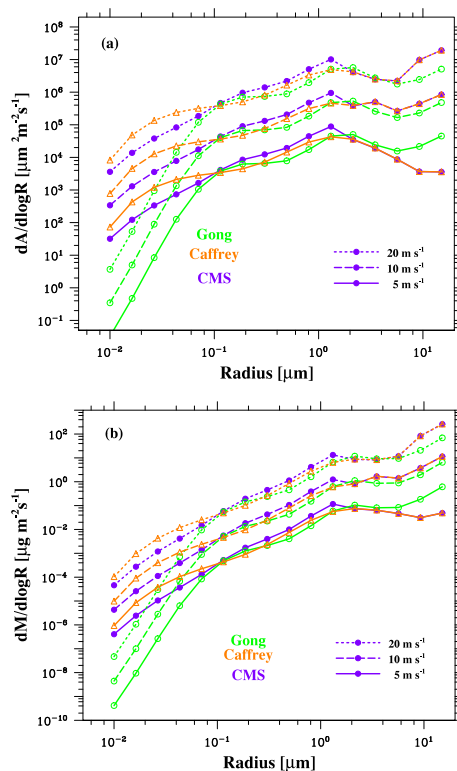


**Fig. 2.** Gong, Caffrey, and CMS source functions shown for **(a)** cross-sectional area and **(b)** mass. The three groups of curves represent the size distribution under wind speed of 5, 10, and  $20 \text{ m s}^{-1}$  from bottom to top. The Caffrey and CMS source functions are corrected for gravitational sedimentation following Hoppel et al. (2005).

Title Page

Abstract

Introduction

Conclusions

References

Tables

Figures

I◀

▶I

◀

▶

Back

Close

Full Screen / Esc

Printer-friendly Version

Interactive Discussion





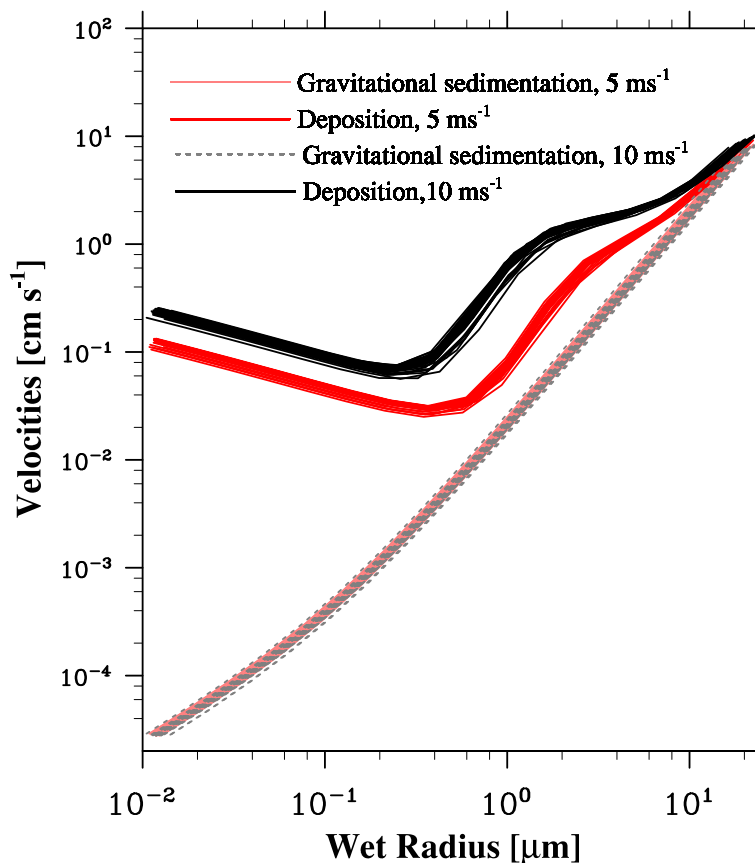


**Fig. 3.** Gravitational velocities and deposition velocities at the grid cells where wind speeds are  $10 \text{ m s}^{-1}$  and  $5 \text{ m s}^{-1}$  over the ocean. Variations of the curves reflect the difference in relative humidity and temperature at different locations. Gravitational velocities at the two wind speeds are overlapped with each other.

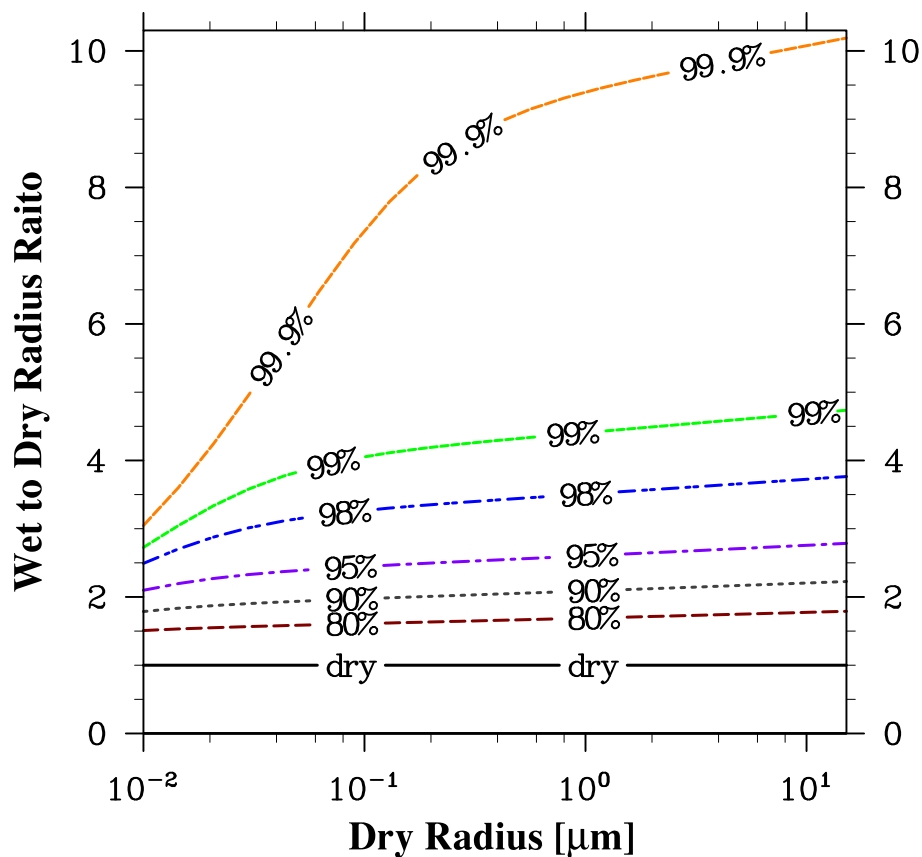


**Fig. 4.** The ratio of wet to dry radius at different relative humidity values using Gerber (1985).

**Modeling sea-salt aerosol**

T. Fan and O. B. Toon

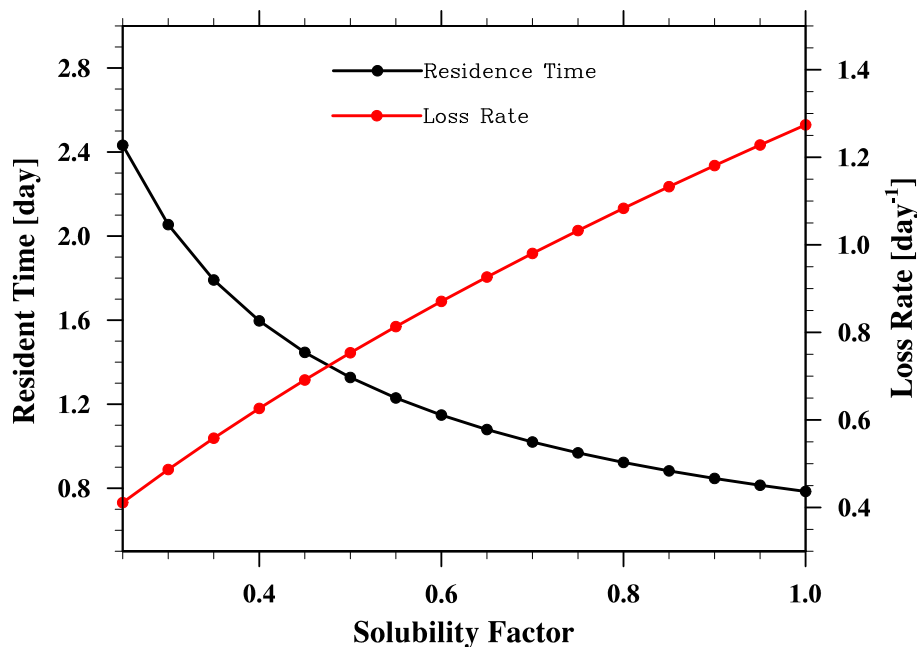


**Fig. 5.** The wet scavenging residence time and loss rate in mass concentration at solubility factors from 0.25 to 1.0.

Title Page

Abstract

Introduction

Conclusions

References

Tables

Figures

◀

▶

◀

▶

Back

Close

Full Screen / Esc

Printer-friendly Version

Interactive Discussion



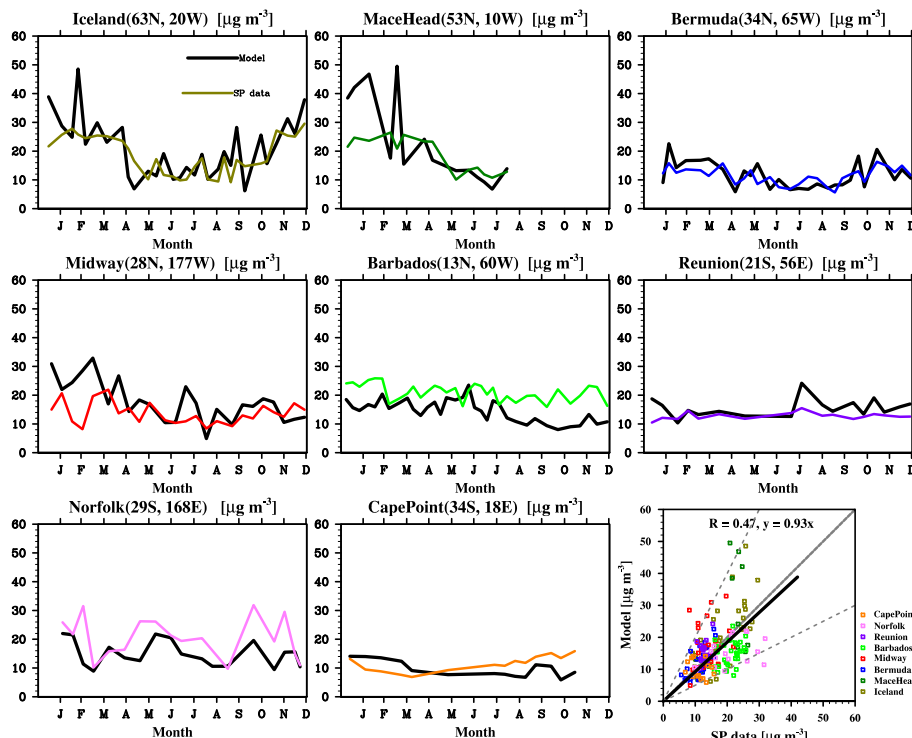


**Fig. 6.** Seasonal variations and scatter plot of mass concentrations in the marine boundary layer comparing the model results to the measurements at eight coastal sites by the University of Miami global network (SP data, Savoie and Prospero, 1977). We used the CMS source function with a solubility factor of 0.5. The solid line in the scatter plot is the total linear fit to all the data. The grey short dash line is the one-to-one line and the grey long dashed lines are the one-to-two and two-to-one lines.

## Modeling sea-salt aerosol

T. Fan and O. B. Toon

Title Page

Abstract

Introduction

Conclusions

References

Tables

Figures

◀

▶

◀

▶

Back

Close

Full Screen / Esc

Printer-friendly Version

Interactive Discussion



**Modeling sea-salt aerosol**

T. Fan and O. B. Toon

Title Page

Abstract

Introduction

Conclusions

References

Tables

Figures

◀

▶

◀

▶

Back

Close

Full Screen / Esc

Printer-friendly Version

Interactive Discussion

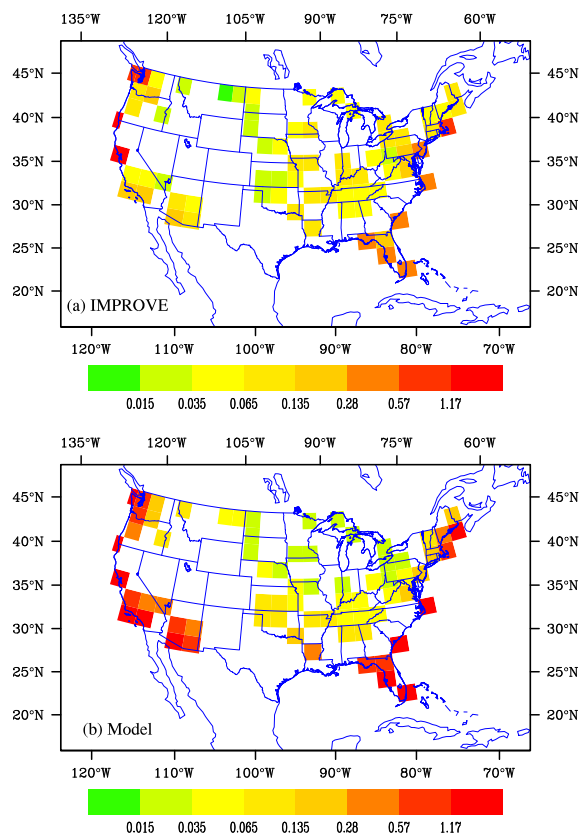


**Fig. 7.** Inland transport of fine mode sea salt mass comparing between **(a)** the IMPROVE dataset and **(b)** the model using the CMS source function with solubility factor of 0.5, unit:  $\mu\text{g m}^{-3}$ . IMPROVE data are the year average of 2006, fine mode ( $\text{PM}_{2.5}$ , diameter  $< 2.5 \mu\text{m}$ ) chloride multiplied by 1.8. Model values are the averages of March, June, September 2006, with upper limit of  $0.95 \mu\text{m}$  in radius.

**Modeling sea-salt aerosol**

T. Fan and O. B. Toon

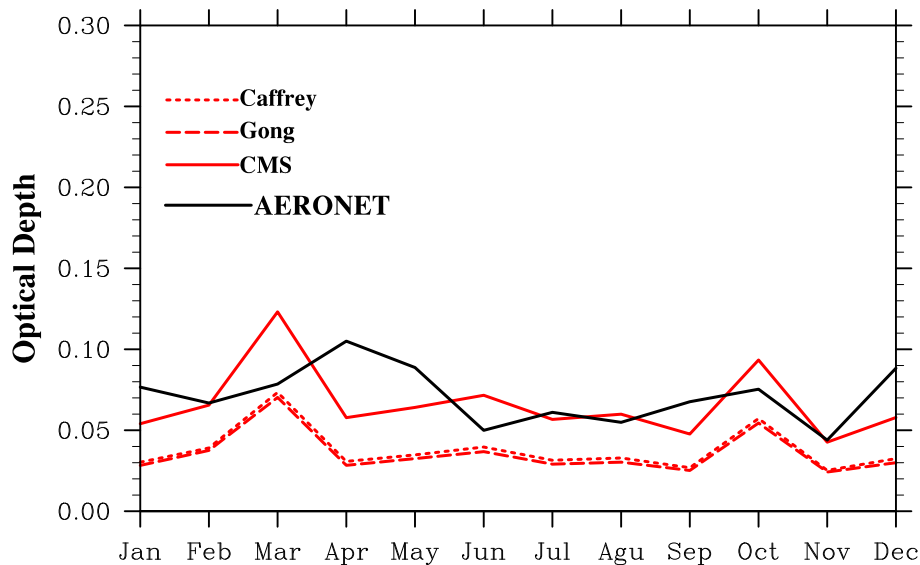


**Fig. 8.** Monthly averaged model and AERONET coarse-mode 500 nm optical depths at Midway Island ( $28^{\circ}$  N,  $177^{\circ}$  W) in 2006. Results using Gong, Caffrey, and CMS source functions are compared here using a solubility factor of 0.5.

[Title Page](#)[Abstract](#)[Introduction](#)[Conclusions](#)[References](#)[Tables](#)[Figures](#)[I◀](#)[▶I](#)[◀](#)[▶](#)[Back](#)[Close](#)[Full Screen / Esc](#)[Printer-friendly Version](#)[Interactive Discussion](#)

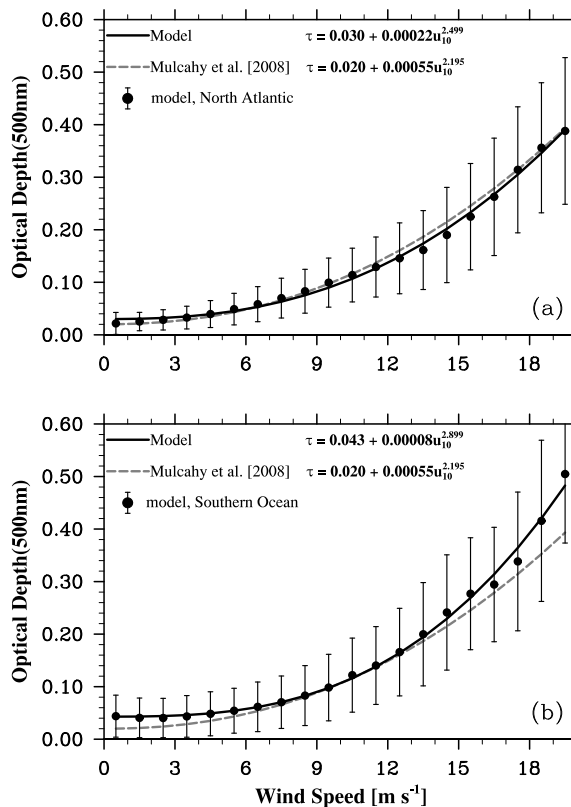


**Fig. 9.** Wind speed dependence of sea salt optical depth in **(a)** North Atlantic and **(b)** roaring forties. Dots are the modeled yearly-averaged optical depths displayed in the middle of the wind speed interval. Error bars represent one standard deviation of the values in the region. The dash lines are the optical depths of the power-law relationship of Mulcahy et al. (2008) using model 10 m wind speed with constant term scaled down to 0.02. The model used the CMS source function and a solubility factor of 0.5.

## Modeling sea-salt aerosol

T. Fan and O. B. Toon

Title Page

Abstract

Introduction

Conclusions

References

Tables

Figures

◀

▶

◀

▶

Back

Close

Full Screen / Esc

Printer-friendly Version

Interactive Discussion



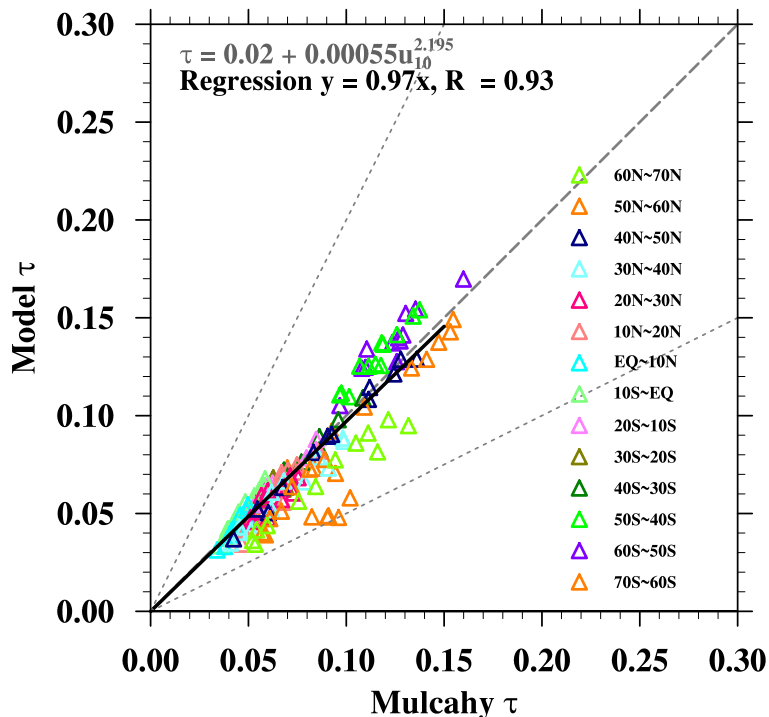


**Fig. 10.** Modeled optical depth model compared with calculated optical depth by Mulcahy et al. (2008) wind speed-optical depth relationship. The slope of the regression line and the correlation ( $R$ ) are shown. The long dash line is the one-to-one line and the short dash lines are one-to-two and two-to-one lines. Each triangle is a monthly-mean of a  $10^\circ$  latitude region. Colors represent the latitudes. The model used the CMS source function and a solubility factor of 0.5.



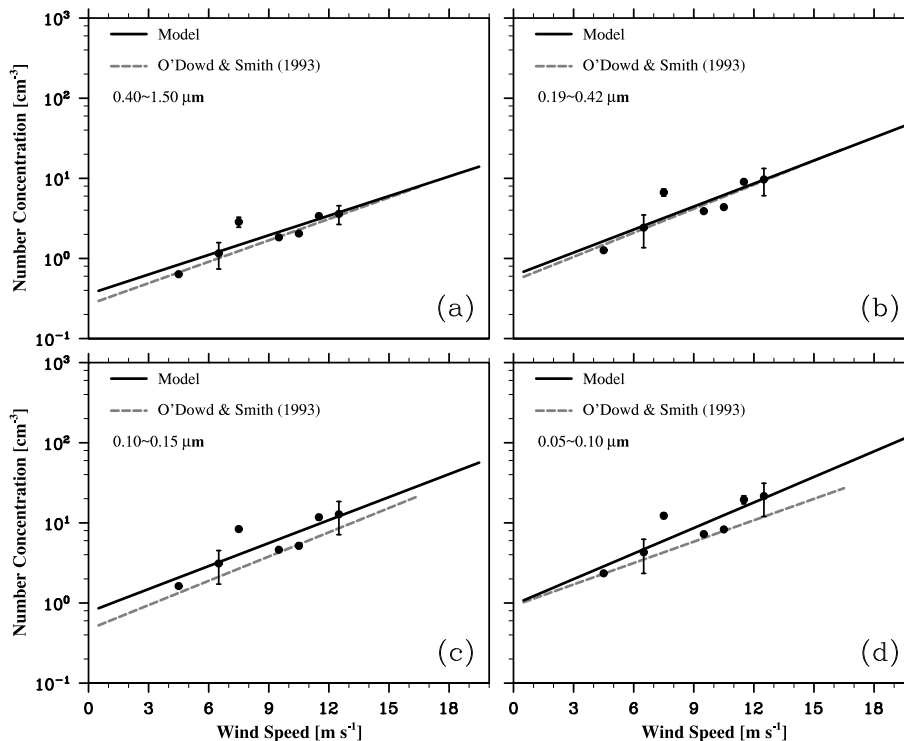


**Fig. 11.** Wind speed dependence of the number concentration in the model compared with measurements by O'Dowd and Smith (1993) in October at Northeast Atlantic (63° N, 8° W) in the size range **(a)** 0.40–1.50  $\mu\text{m}$ , **(b)** 0.19–0.42  $\mu\text{m}$ , **(c)** 0.10–0.15  $\mu\text{m}$ , and **(d)** 0.05–0.10  $\mu\text{m}$ . The dots are the modeled number with error bars representing one standard deviation. The solid lines are the linear fits. The model used the CMS source function and a solubility factor of 0.5.

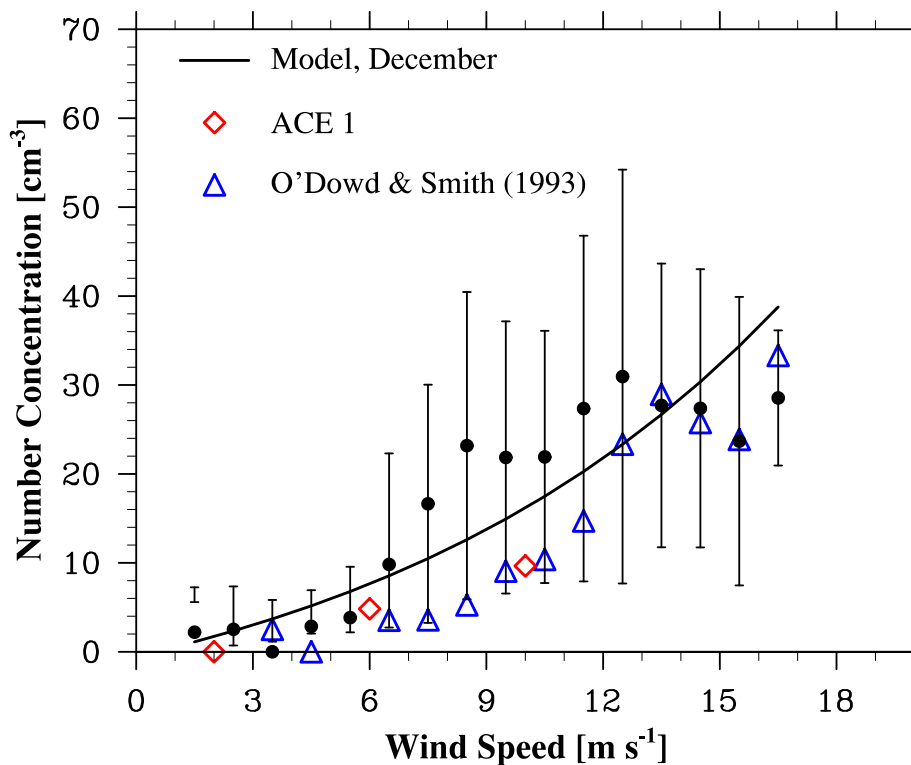


**Fig. 12.** Wind dependence of number concentration of the model in the South Pacific compared to the function of O'Dowd and Smith (1993) and the ACE-1 data. The error bars represent one standard deviation of the model results. The model and O'Dowd and Smith data are for radius 0.05–0.15  $\mu\text{m}$  and 0.19–0.42  $\mu\text{m}$ . The ACE-1 data are for radius 0.075–0.5  $\mu\text{m}$ . The model used the CMS source function and a solubility factor of 0.5.

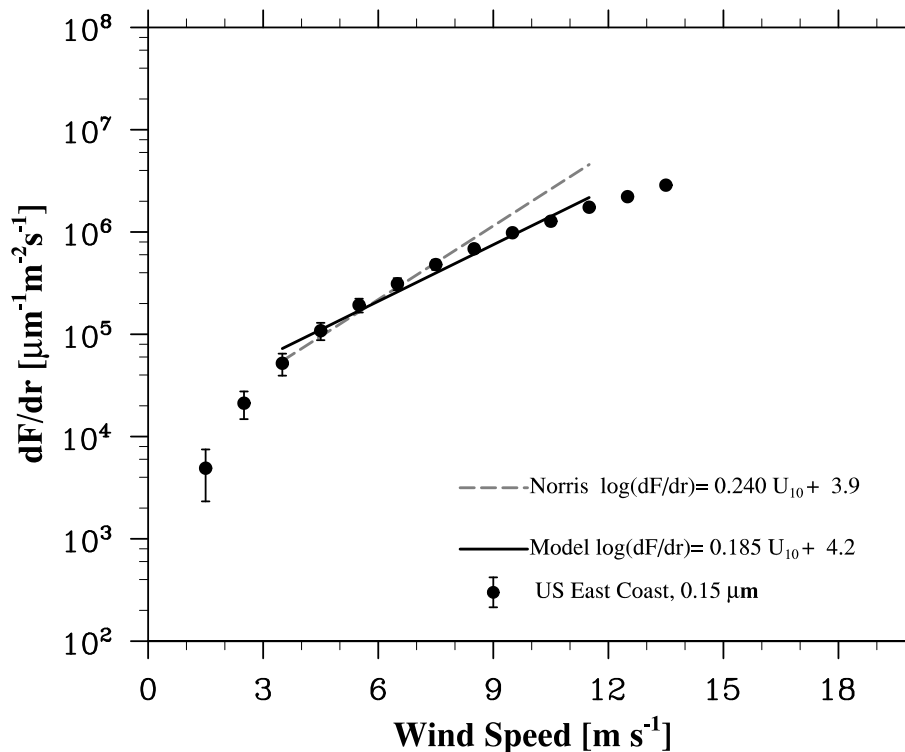


**Fig. 13.** Emission fluxes of 0.15 μm radius sea salt at different wind speeds. The dots with error bars are the model parameterized emission fluxes. The solid line is the log-linear fit for wind speed range 4–12  $\text{m s}^{-1}$ . The dashed line is the emission flux by Norris et al. (2008). The model values were averaged over the area of ship measurement at the United States east coast (24–36° N, 50–77° W). The model used the CMS source function and a solubility factor of 0.5.

# Modeling sea-salt aerosol

T. Fan and O. B. Toon

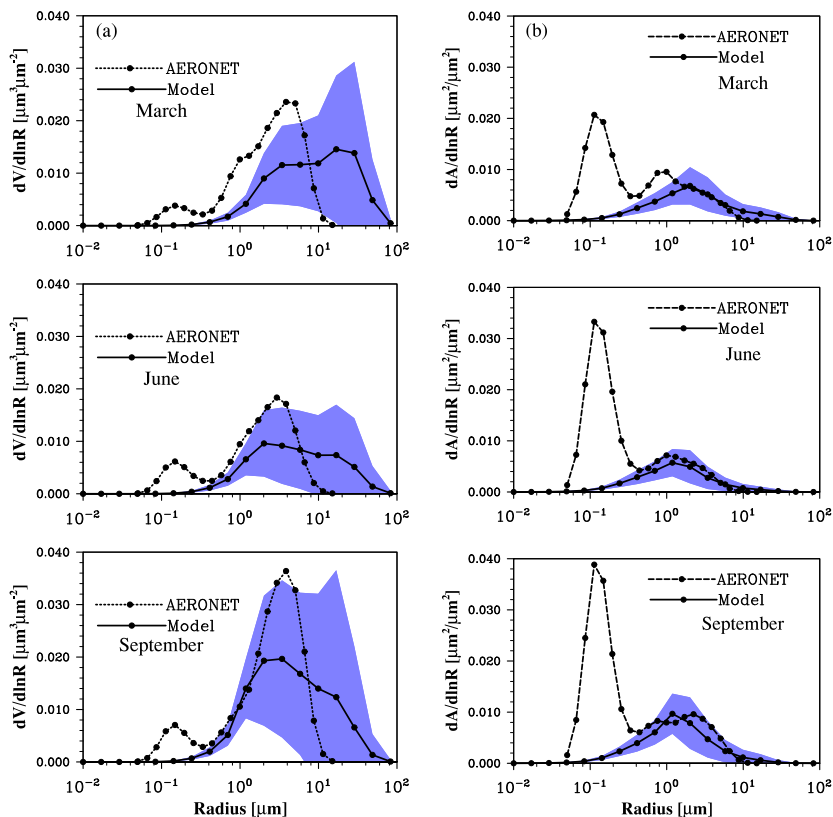


**Fig. 14.** (a) volumetric size distribution compared between the model and AERONET inversion product at Midway Island in March, June, and September 2006. The shaded area around the model curve is one standard deviation of all the daily size distributions; (b) same as (a) but for cross-sectional area size distribution. The model results are vertically integrated. The model used the CMS source function and a solubility factor of 0.5.

Title Page

Abstract

Introduction

Conclusions

References

Tables

Figures

◀

▶

◀

▶

Back

Close

Full Screen / Esc

Printer-friendly Version

Interactive Discussion



**Modeling sea-salt aerosol**

T. Fan and O. B. Toon

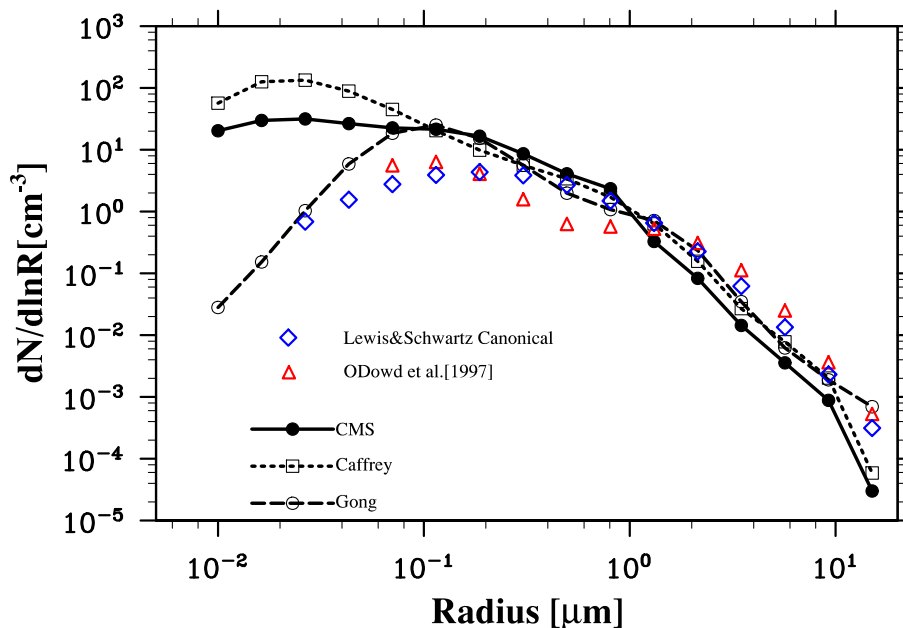


**Fig. 15.** Surface number size distribution compared between the modeled distribution and O'Dowd et al. (1993) empirical relationship and Lewis and Schwartz (2004) canonical distribution at Midway Island in June 2006. The model used a solubility factor of 0.5.

[Title Page](#)[Abstract](#)[Introduction](#)[Conclusions](#)[References](#)[Tables](#)[Figures](#)[◀](#)[▶](#)[◀](#)[▶](#)[Back](#)[Close](#)[Full Screen / Esc](#)[Printer-friendly Version](#)[Interactive Discussion](#)

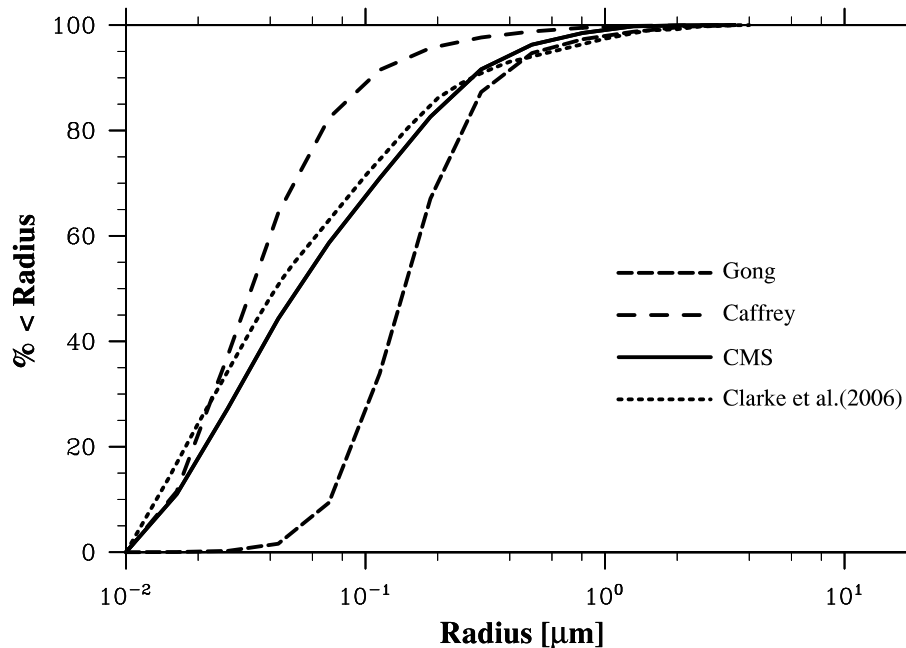


**Fig. 16.** Percentage of number concentration with dry radius larger than the value indicated in the model bottom layer compared between model results using Gong, Caffrey and CMS source function and Clarke et al. (2006). The model size distributions are from the grid cell containing the Midway Island in June 2006. The model used a solubility factor of 0.5.

## Modeling sea-salt aerosol

T. Fan and O. B. Toon

Title Page

Abstract

Introduction

Conclusions

References

Tables

Figures

◀

▶

◀

▶

Back

Close

Full Screen / Esc

Printer-friendly Version

Interactive Discussion



**Modeling sea-salt aerosol**

T. Fan and O. B. Toon

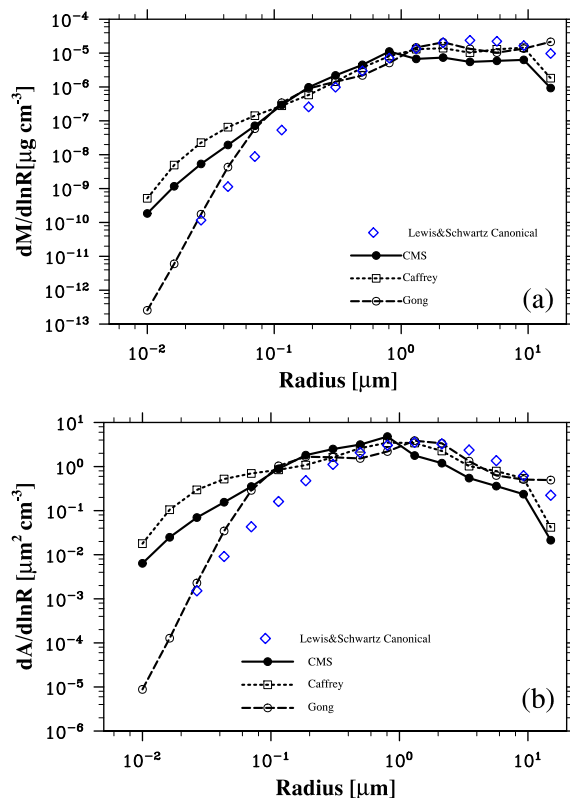


**Fig. 17.** Same as Fig. 15 except for (a) mass and (b) cross-sectional area size distribution.

Title Page

Abstract

Introduction

Conclusions

References

Tables

Figures

◀

▶

◀

▶

Back

Close

Full Screen / Esc

Printer-friendly Version

Interactive Discussion



# Modeling sea-salt aerosol

T. Fan and O. B. Toon

Title Page

Abstract

Introduction

Conclusions

References

Tables

Figures

◀

▶

◀

▶

Back

Close

Full Screen / Esc

Printer-friendly Version

Interactive Discussion

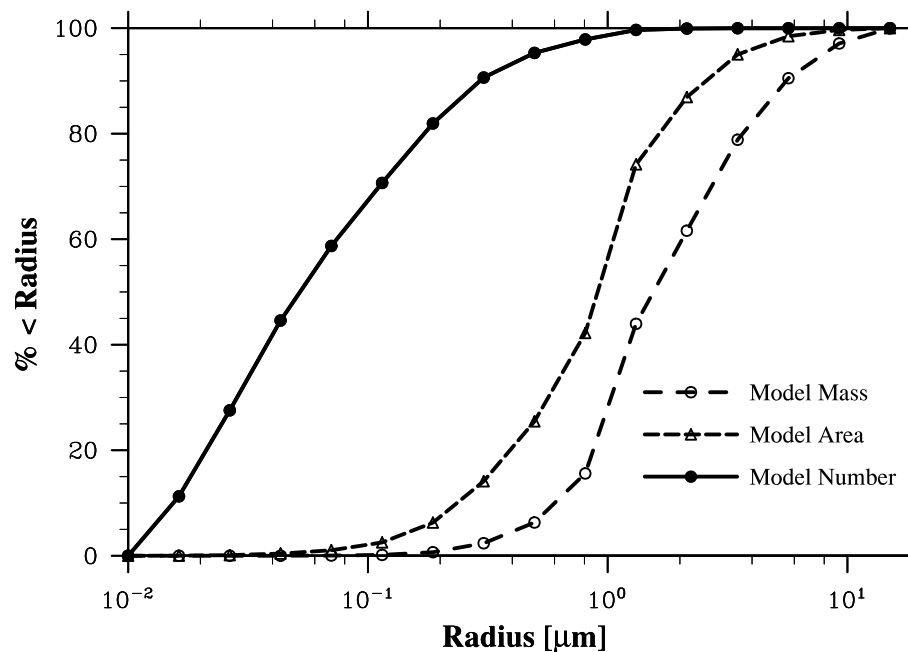


**Fig. 18.** Percentage of number, cross-sectional area, and mass size distribution in dry radius of 0.01–15.2  $\mu\text{m}$ . The number and mass concentration are for bottom layer. The cross-sectional area is calculated for humidified particles in the whole column. These are the size distributions at Midway Island in June 2006 using the CMS source function and a solubility factor of 0.5.



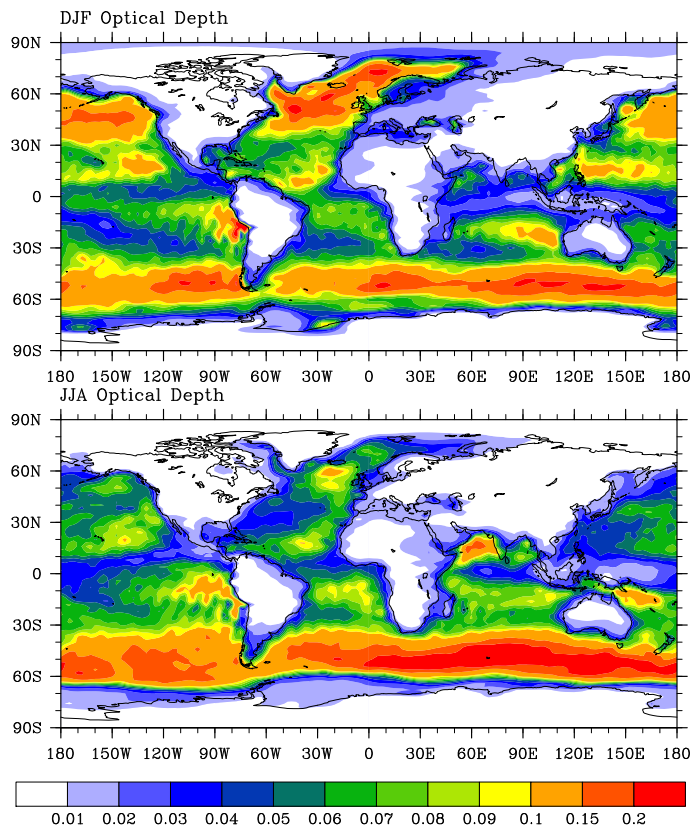


**Fig. 19.** Modeled global distribution of SSA optical depth and number concentration in the boreal winter (DJF, December, January, and February) and summer (JJA, June, July, and August) of 2006. The model used the CMS source function and a solubility factor of 0.5.

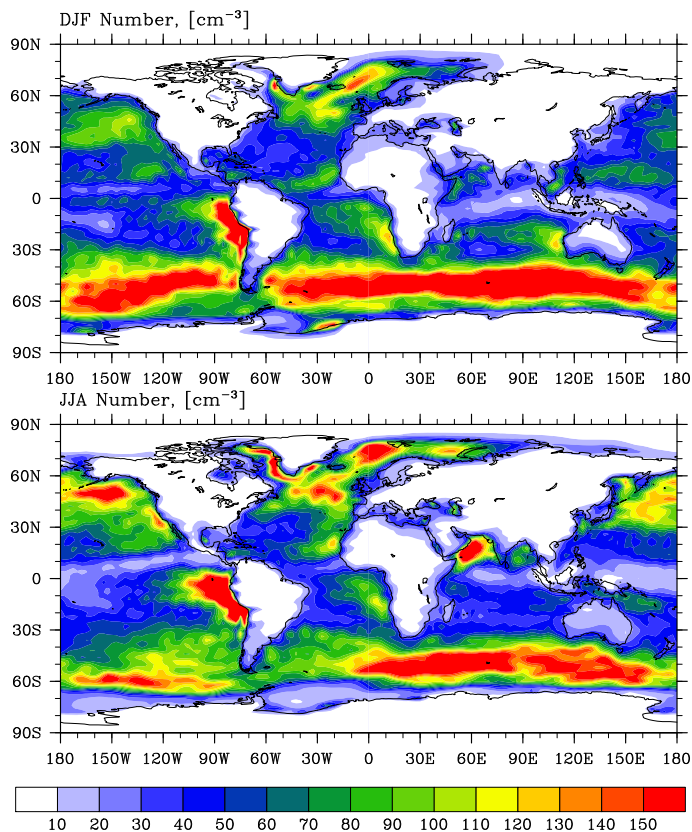


**Fig. 20.** Modeled global distribution of SSA number concentration in the boreal winter (DJF, December, January, and February) and summer (JJA, June, July, and August) of 2006. The model used the CMS source function and a solubility factor of 0.5.

# Modeling sea-salt aerosol

T. Fan and O. B. Toon

Title Page

Abstract

Introduction

Conclusions

References

Tables

Figures

◀

▶

◀

▶

Back

Close

Full Screen / Esc

Printer-friendly Version

Interactive Discussion

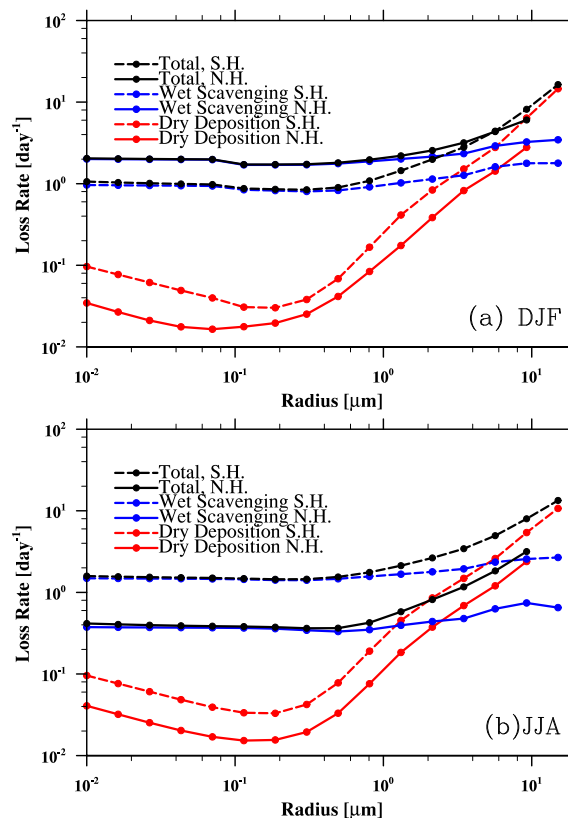


**Fig. 21.** The dry deposition, wet scavenging and total loss rate of particles as a function of radius for 30–60° N (Northern Hemisphere, N.H.) and 30–60° S (Southern Hemisphere, S.H.) in **(a)** June, July, and August (JJA) and **(b)** December, January, February (DJF). The model used a solubility factor of 0.5.

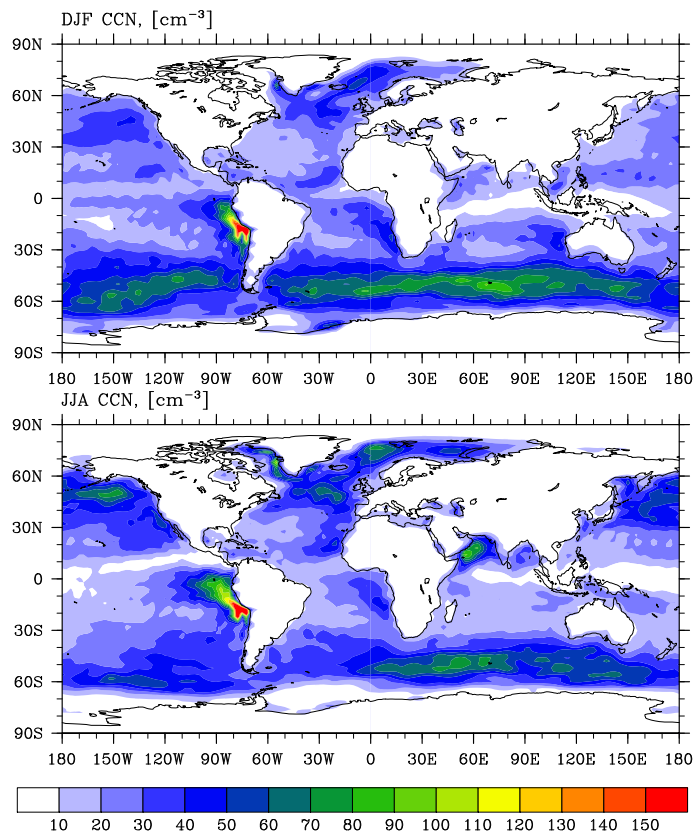


**Fig. 22.** Modeled global distribution of marine boundary layer CCN at supersaturation of 0.1% in the boreal winter (DJF, December, January, and February) and summer (JJA, June, July, and August) of 2006. The model used the CMS source function and a solubility factor of 0.5.